CrossMark

J. Fluid Mech. (2017), *vol.* 816, *pp.* 719–745. © Cambridge University Press 2017
doi:10.1017/jfm.2017.103

Nonlinear mode interactions in a counter-rotating split-cylinder flow

Paloma Gutierrez-Castillo[1] **and Juan M. Lopez**[1,†]

[1]School of Mathematical and Statistical Sciences, Arizona State University, Tempe, AZ 85287, USA

(Received 11 November 2016; revised 9 February 2017; accepted 10 February 2017;
first published online 10 March 2017)

The flow in a split cylinder with each half in exact counter rotation is studied numerically. The exact counter rotation, quantified by a Reynolds number Re based on the rotation rate and radius, imparts the system with an $O(2)$ symmetry (invariance to azimuthal rotations as well as to an involution consisting of a reflection about the mid-plane composed with a reflection about any meridional plane). The $O(2)$ symmetric basic state is dominated by a shear layer at the mid-plane separating the two counter-rotating bodies of fluid, created by the opposite-signed vortex lines emanating from the two endwalls being bent to meet at the split in the sidewall. With the exact counter rotation, the additional involution symmetry allows for steady non-axisymmetric states, that exist as a group orbit. Different members of the group simply correspond to different azimuthal orientations of the same flow structure. Steady states with azimuthal wavenumber m (the value of m depending on the cylinder aspect ratio Γ) are the primary modes of instability as Re and Γ are varied. Mode competition between different steady states ensues, and further bifurcations lead to a variety of different time-dependent states, including rotating waves, direction-reversing waves, as well as a number of slow–fast pulse waves with a variety of spatio-temporal symmetries. Further from the primary instabilities, the competition between the vortex lines from each half-cylinder settles on either a $m=2$ steady state or a limit cycle state with a half-period-flip spatio-temporal symmetry. By computing in symmetric subspaces as well as in the full space, we are able to unravel many details of the dynamics involved.

Key words: bifurcation, nonlinear dynamical systems, nonlinear instability

1. Introduction

Flows driven between differentially rotating disks have a long history due to their relevance to many processes in nature and technology, as well as being of fundamental interest (Batchelor 1951; Stewartson 1953; Rott & Lewellen 1966; Zandbergen & Dijkstra 1987; Lopez 1998; Launder, Poncet & Serre 2010). The fundamental issue concerning the nature of the bulk flow between differentially rotating disks depends critically on the lateral conditions at large radii, and for enclosed systems, the sidewall boundary condition plays a major role in determining the bulk flow, due to the induced meridional flow. For the most part, these types of

† Email address for correspondence: juan.m.lopez@asu.edu

https://doi.org/10.1017/jfm.2017.103 Published online by Cambridge University Press

flows have been studied in cylindrical containers, and when the differential rotation is sufficiently strong, the axisymmetry of the flow is broken leading to rotating waves, modulated rotating waves and other spatio-temporally complicated states (Blackburn & Lopez 2000, 2002; Gauthier *et al.* 2002; Lopez *et al.* 2002; Marques, Gelfgat & Lopez 2003; Lopez & Marques 2004; Moisy *et al.* 2004; Lopez 2006).

The case when the two endwalls (disks) are exactly in counter rotation and the sidewall is stationary, the so-called von Kármán swirling flow, is special as the system is more than just axisymmetric (invariance to rotations about the axis, $SO(2)$ symmetry), it is also invariant to a Z_2 symmetry (involution). This involution is a combination of a reflection through any meridional plane composed with a reflection about the mid-plane (Nore *et al.* 2003, 2004, 2006), and is equivalent to a rotation of π about an axis through the centre of the cylinder that is orthogonal to the cylinder axis. This involution does not commute with the rotation, and together these symmetries form an $O(2)$ symmetry group. In general, differentially rotating cylinder flows only have $SO(2)$ symmetry, and it is well established that flows with $O(2)$ symmetry can have fundamentally different behaviour to flows with $SO(2)$ symmetry (Crawford & Knobloch 1991; Knobloch 1996). In particular, when axisymmetry is broken in an $SO(2)$ system, rotating waves result, whereas in $O(2)$ systems, steady three-dimensional states can result.

The flow in a cylinder with exactly counter-rotating endwalls and a stationary sidewall, the von Kármán swirling flow, has attracted much attention as a possible laboratory-scale dynamo. The motivation comes from the torsional forcing of the counter-rotating endwalls providing a global-scale dynamo action. However, the stationary sidewall imparts significant viscous drag, substantially reducing the effectiveness of the counter-rotating endwalls driving a torsional flow. Experimentally, the flat endwalls are replaced by impellers to counteract the sidewall effects (Bourgoin *et al.* 2002; Ravelet *et al.* 2004; Monchaux *et al.* 2007; de la Torre & Burguete 2007; Ravelet *et al.* 2008; Crespo del Arco *et al.* 2009; Giesecke, Stefani & Burguete 2012). The $O(2)$ symmetry of the problem leads to interesting dynamics when it is broken, resulting from mode interactions which have strong spatial resonances. Nore *et al.* (2003) studied the competition between states with azimuthal wavenumbers $m = 1$ and 2. Such $1:2$ resonances have drawn considerable attention from a dynamical systems perspective as there are associated robust heteroclinic cycles in reduced-order models (normal form equations) of such systems (Dangelmayr 1986; Jones & Proctor 1987; Armbruster, Guckenheimer & Holmes 1988; Krupa 1990; Porter & Knobloch 2001). In particular, Nore *et al.* (2003) have found slow–fast dynamic states that they have associated with the heteroclinic cycles in the normal form model. Nore, Moisy & Quartier (2005) have observed such states in experiments, the so-called near-heteroclinic cycles, albeit influenced to some degree by noise and geometrical defects.

Here, we study a flow related to the von Kármán swirling flow, with the essential difference being that instead of having a stationary sidewall, the sidewall is split at the half-height, with each half rotating with the corresponding endwall. This flow has significantly less sidewall drag on the global torsional flow since the split sidewall halves also counter rotate at the same rate as their corresponding endwalls, and so may provide an enhanced dynamo action. This configuration has the same $O(2)$ symmetry as the von Kármán swirling flow, but the shear at mid-height is much stronger for the same aspect ratio and rotation rates of the endwalls. As in the von Kármán swirling flow, the primary instabilities are dominated by the dynamics associated with $O(2)$ symmetry breaking, mode interactions and competitions, but in the split sidewall flow

https://doi.org/10.1017/jfm.2017.103 Published online by Cambridge University Press

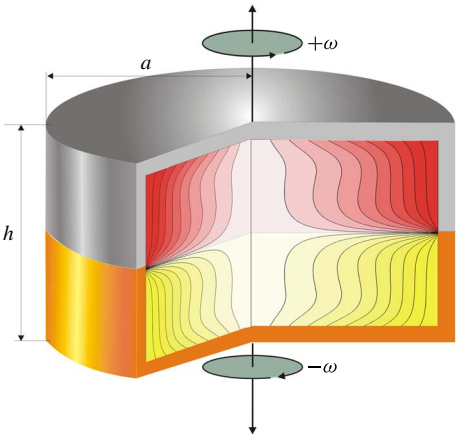


FIGURE 1. (Colour online) Schematic of the flow system. The inset shows contours of rv (vortex lines) for a basic state at $(\Gamma, Re) = (1, 115)$. There are ten quadratically spaced contour levels of $rv \in [-Re, Re]$, with positive being red and negative being yellow.

these occur at significantly lower Reynolds numbers (non-dimensional endwall rotation rates). Over a considerable portion of the range of Reynolds numbers and aspect ratios considered, the dynamics is dominated by pulse wave states that are associated with the $O(2)$ symmetry breaking.

2. Governing equations and numerical methods

The flow of a fluid of kinematic viscosity ν contained in a rotating split cylinder is studied numerically. The cylinder of radius a and length h is split in two at mid-height and the two halves are counter-rotating with angular speeds $\pm\omega$. A schematic of the problem is shown in figure 1. Using a as the length scale and a^2/ν as the time scale, the non-dimensional Navier–Stokes equations are

$$(\partial_t + \boldsymbol{u}\cdot\boldsymbol{\nabla})\boldsymbol{u} = -\boldsymbol{\nabla}p + \nabla^2\boldsymbol{u}, \quad \boldsymbol{\nabla}\cdot\boldsymbol{u} = 0. \tag{2.1a,b}$$

The no-slip boundary conditions are:

$$\left.\begin{aligned} (u, v, w) = (0, rRe, 0) \text{ at the top endwall, } z = 0.5\Gamma, \\ (u, v, w) = (0, -rRe, 0) \text{ at the bottom endwall, } z = -0.5\Gamma, \\ (u, v, w) = (0, Re, 0) \text{ at the top half of the sidewall, } r = 1, z \in (0, 0.5\Gamma), \\ (u, v, w) = (0, -Re, 0) \text{ at the bottom half of the sidewall, } r = 1, z \in (-0.5\Gamma, 0), \end{aligned}\right\} \tag{2.2}$$

where the two governing parameters are

$$\left.\begin{aligned} &\text{aspect ratio:} && \Gamma = h/a, \\ &\text{Reynolds number:} && Re = \omega a^2/\nu. \end{aligned}\right\} \tag{2.3}$$

In polar coordinates $(r, \theta, z) \in [0, 1] \times [0, 2\pi] \times [-0.5\Gamma, 0.5\Gamma]$, the velocity is $\boldsymbol{u} = (u, v, w)$ and the vorticity is $\boldsymbol{\nabla}\times\boldsymbol{u} = (\chi, \eta, \zeta) = (w_\theta/r - v_z, u_z - w_r, v_r + v/r - u_\theta/r)$.

The Navier–Stokes equations are solved using a spectral code based on Mercader, Batiste & Alonso (2010), using a second-order time-splitting method and space

https://doi.org/10.1017/jfm.2017.103 Published online by Cambridge University Press

discretized via a Galerkin–Fourier expansion in θ and Chebyshev collocation in r and z:

$$\boldsymbol{u}(r,\theta,z,t)=\sum_{i=0}^{2n_r+1}\sum_{j=0}^{n_z}\sum_{k=-0.5n_\theta}^{k=0.5n_\theta-1}\hat{\boldsymbol{u}}_{ijk}(t)\,\Xi_i(r)\,\Xi_j(2z/\Gamma)\mathrm{e}^{\mathrm{i}k\theta}, \tag{2.4}$$

where Ξ_n is the nth Chebyshev polynomial. The modal kinetic energies corresponding to azimuthal wavenumbers m are

$$E_m=\frac{1}{2}\int_{-0.5\Gamma}^{0.5\Gamma}\int_0^1 \boldsymbol{u}_m\cdot\boldsymbol{u}_m^* r\,\mathrm{d}r\,\mathrm{d}z, \tag{2.5}$$

where $\boldsymbol{u}_m$ is the mth Fourier component of the velocity field and $\boldsymbol{u}_m^*$ is its complex conjugate.

To avoid Gibb's phenomenon due to the discontinuity in the sidewall boundary condition for the azimuthal velocity, we regularized the boundary condition by smoothing the discontinuity over a small distance. Specifically, we replaced the boundary condition for the azimuthal velocity with

$$v(r=1,\theta,z)=Re\tanh(\epsilon z), \tag{2.6}$$

where ϵ governs the distance over which the jump is smoothed; $\epsilon=50$ was used in this study, as was done in related rotating split-cylinder problems (Gutierrez-Castillo & Lopez 2015; Lopez & Gutierrez-Castillo 2016). A spatial resolution of $n_r=40$, $n_z=160$ and $n_\theta=64$, and a time resolution of $\delta_t\in[10^{-4},10^{-5}]$ was used for the parameter range studied, $\Gamma\in[0.5,2.0]$ and $Re\in[100,300]$. In this parameter range, the resolution used results in spectral convergence in the coefficients in (2.4) of over sixteen orders of magnitude in θ, six orders of magnitude in r and three orders of magnitude in z. The slower convergence in z is due to using the L_∞ norm; the convergence is slowest in the neighbourhood of the sidewall split, but this slow convergence is very localized and constrained by the viscous boundary layer. The convergence in z away from the split is comparable to that in r. Also, with this resolution, there are at least 15 collocation points across boundary layers, resulting in very well resolved solutions. Figure 2 illustrates how well the solutions are resolved by presenting the axial velocity profiles of the three velocity components at $r=0.5$ and $\theta=0$ of a typical state, S2 at $(\Gamma,Re)=(1.45,123)$, computed with $n_r=40$, $n_\theta=64$ and either $n_z=120$ (thick black curves) or $n_z=160$ (thin coloured curves). On the scale of the plot, the two solutions are indistinguishable. Also shown in the figure are the absolute differences between the three velocity components computed with the two resolutions, showing that the difference resulting from a 33 % increase in the axial resolution, from $n_z=120$ to $n_z=160$, only affects the solution in the fifth significant digit in the interior.

The system (2.1) and (2.2) is invariant to two spatial symmetries and a time translation $\mathcal{T}_\beta$. One spatial symmetry is $\mathcal{R}_\alpha$, the invariance to arbitrary rotations about the cylinder axis. It is isomorphic to the $SO(2)$ symmetry group. The other spatial symmetry is $\mathcal{H}_\gamma$, the combined action of a reflection in any meridional plane $\theta=\gamma$ and a reflection in the mid-plane $z=0$. This combined reflection is equivalent to a rotation of π about a direction through the centre of the cylinder that is orthogonal to the cylinder axis and in the $\theta=\gamma$ plane. The $\mathcal{H}_\gamma$ involution is isomorphic to the

https://doi.org/10.1017/jfm.2017.103 Published online by Cambridge University Press

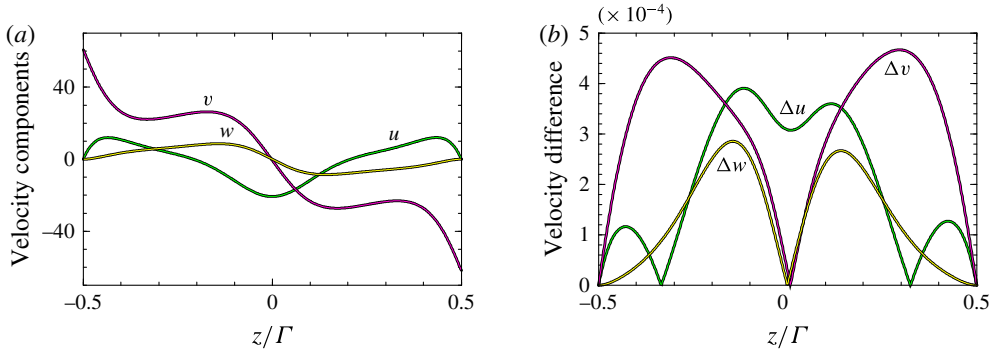


FIGURE 2. (Colour online) (*a*) Axial (z) profiles of the three velocity components at $r = 0.5$ and $\theta = 0$ of S2 at $(\Gamma, Re) = (1.45, 123)$ computed with $n_r = 40$, $n_\theta = 64$ and either $n_z = 120$ (thick black curves) or $n_z = 160$ (thin coloured curves), and (*b*) the absolute differences between the three velocity component computed with the two resolutions.

State	Symmetries
Basic state (BS)	$\mathcal{R}_\alpha \boldsymbol{u} = \boldsymbol{u},\ \mathcal{H}_\gamma \boldsymbol{u} = \boldsymbol{u},\ \mathcal{T}_\beta \boldsymbol{u} = \boldsymbol{u}$
Steady $\mathcal{H}$-symmetric states (Sm)	$\mathcal{R}_{2\pi/m} \boldsymbol{u} = \boldsymbol{u},\ \mathcal{H}_\gamma \boldsymbol{u} = \boldsymbol{u}$ for $2m$ angles γ, $\mathcal{T}_\beta \boldsymbol{u} = \boldsymbol{u}$
Rotating waves (RW)	$\mathcal{R}_\pi \boldsymbol{u} = \boldsymbol{u},\ \mathcal{R}_\alpha \boldsymbol{u} = \mathcal{T}_{(\alpha T_w)/2\pi} \boldsymbol{u},\ \mathcal{T}_{T_w} \boldsymbol{u} = \boldsymbol{u}$
Direction-reversing waves (DRW)	$\mathcal{R}_{\pi/2} \boldsymbol{u} = \boldsymbol{u},\ \mathcal{T}_{T_E} \boldsymbol{u} = \boldsymbol{u}$
Pulse waves (PWs)	$\mathcal{R}_\pi \boldsymbol{u} = \boldsymbol{u},\ \mathcal{R}_\alpha \boldsymbol{u} = \mathcal{T}_{T_E} \boldsymbol{u}$; α not a rational fraction of π
Pulse waves (PWa)	$\mathcal{R}_\alpha \boldsymbol{u} = \mathcal{T}_{T_E} \boldsymbol{u}$; α not a rational fraction of π
Pulse waves (PWo)	$\mathcal{R}_\pi \boldsymbol{u} = \boldsymbol{u},\ \mathcal{T}_{2T_E} \boldsymbol{u} = \boldsymbol{u},\ \mathcal{T}_{T_E} \boldsymbol{u} = \mathcal{R}_{\phi-2\gamma} \mathcal{H}_\gamma \boldsymbol{u}$ for a given ϕ
Limit cycles (LC)	$\mathcal{T}_{2T_E} \boldsymbol{u} = \boldsymbol{u},\ \mathcal{T}_{T_E} \boldsymbol{u} = \mathcal{R}_{\phi-2\gamma} \mathcal{H}_\gamma \boldsymbol{u}$ for a given ϕ

TABLE 1. Summary of the different states and their symmetries. Note that α, γ and β are arbitrary unless otherwise indicated.

Z_2 symmetry group; applying it twice is equivalent to the identity operation. The actions of $\mathcal{R}_\alpha$, $\mathcal{H}_\gamma$, and $\mathcal{T}_\beta$ on the velocity are

$$\left.\begin{aligned} \mathcal{R}_\alpha(u, v, w)(r, \theta, z, t) &= (u, v, w)(r, \theta + \alpha, z, t), \quad \alpha \text{ arbitrary}, \\ \mathcal{H}_\gamma(u, v, w)(r, \theta, z, t) &= (u, -v, -w)(r, 2\gamma - \theta, -z, t), \quad \gamma \text{ arbitrary}, \\ \mathcal{T}_\beta(u, v, w)(r, \theta, z, t) &= (u, v, w)(r, \theta, z, t + \beta), \quad \beta \text{ arbitrary}. \end{aligned}\right\} \tag{2.7}$$

The two spatial symmetries, $\mathcal{R}_\alpha$ and $\mathcal{H}_\gamma$, do not commute, and together they are isomorphic to the $O(2)$ symmetry group.

Much of the nonlinear dynamics involves the breaking of some aspects of the symmetries of the problem. Table 1 lists the various states encountered in this study together with their symmetries. Each is described in detail in the following section. It is useful to be able to compute the unstable flows following the symmetry-breaking bifurcations. This can be readily done by restricting the computations to invariant symmetric subspaces. The most useful subspaces for this problem are the subspaces ξ_m, in which the flow is restricted to only having azimuthal wavenumbers $m = 0$ and multiples of m. Numerically, this is done by setting to zero the coefficients $\hat{\boldsymbol{u}}_{ijk}$ in (2.4) which do not correspond to these wavenumbers. There are two special such subspaces, ξ_0 which is the axisymmetric subspace and ξ_1 which is the full space.

https://doi.org/10.1017/jfm.2017.103 Published online by Cambridge University Press

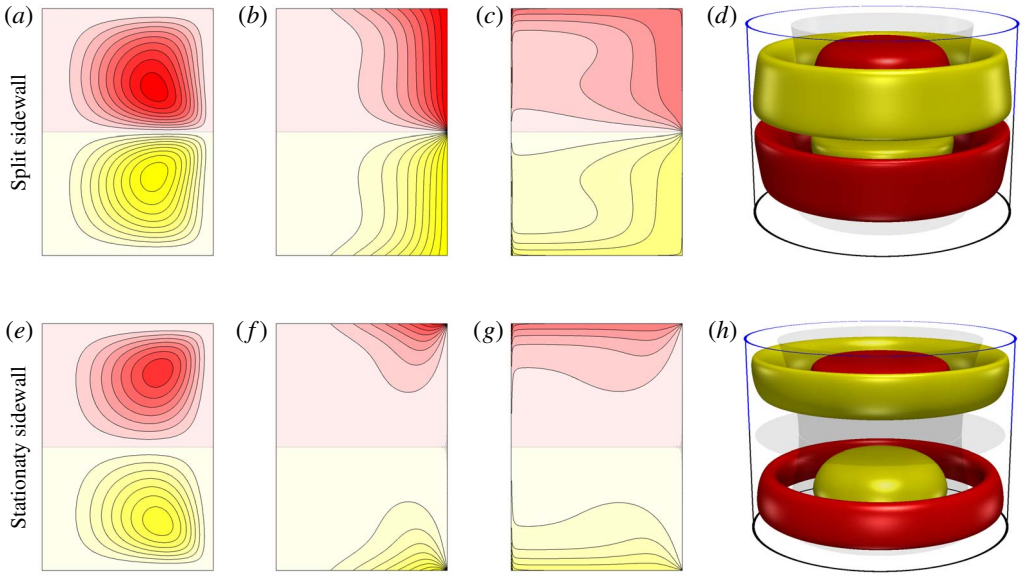


FIGURE 3. (Colour online) Contours in a meridional plane ($\theta = 0$, $r \times z \in [0, 1] \times [-0.5\Gamma, 0.5\Gamma]$) of ($a$) ψ (streamlines), (b) rv (vortex lines), (c) v/r (angular velocity) and (d) isosurfaces of w of BS at $(\Gamma, Re) = (1.45, 115)$ for the split sidewall case (a–d) and the stationary sidewall case (e–h). The contour levels are linearly spaced (positive are red and negative are yellow) in the intervals $\psi \in [-1.25, 1.25]$, $rv \in [-Re, Re]$ and $v/r \in [-2Re, 2Re]$; the isosurfaces are at $w = \pm 0.05Re$ and at $w = 0$ (translucent).

3. Results

In the following subsections, we begin describing the features of the basic state, and consider its primary instabilities to group orbits of steady states. Then, we study in detail the 2 : 3 mode interaction, primarily in the neighbourhood of the codimension-two (codim-2) point at $(\Gamma, Re) = (1.30, 129.5)$, and how some of the secondary bifurcation curves from that codim-2 point connect to the other 2 : 3 codim-2 point at $(\Gamma, Re) = (1.77, 118.6)$. We then consider in detail the dynamics as Re is increased while keeping $\Gamma = 1.45$ fixed. By computing not only in the full three-dimensional space ξ_1, but also by restricting the simulations to various symmetry subspaces ξ_m, we are able to provide a fairly complete picture of the complex dynamics involved. Finally, we provide a general overview of the various mode interactions and subsequent nonlinear dynamics over the broader parameter regime with $\Gamma \in [0.5, 2.0]$ and $Re \in [100, 300]$.

3.1. *Basic state*

The basic state, BS, is invariant to all symmetries of the system; it is steady and $O(2)$ symmetric. The streamlines (contours of ψ, where $u = -1/r\,\partial\psi/\partial z$ and $w = 1/r\,\partial\psi/\partial r$), vortex lines (contours of rv), contours of angular velocity v/r and isosurfaces of the axial velocity w of a typical BS at $(\Gamma, Re) = (1.45, 115)$ are shown in the top row of figure 3. Note that for an axisymmetric velocity $(u, v, w) = (-1/r\,\partial\psi/\partial z,\ v,\ 1/r\,\partial\psi/\partial r)$ and the corresponding vorticity is $(-1/r\,\partial(rv)/\partial z,\ \eta,\ 1/r\,\partial(rv)/\partial r)$, so that vortex lines in a meridional plane are tangent to the isocontours of rv. The dominant feature of BS is the shear layer formed at the cylinder mid-height

https://doi.org/10.1017/jfm.2017.103 Published online by Cambridge University Press

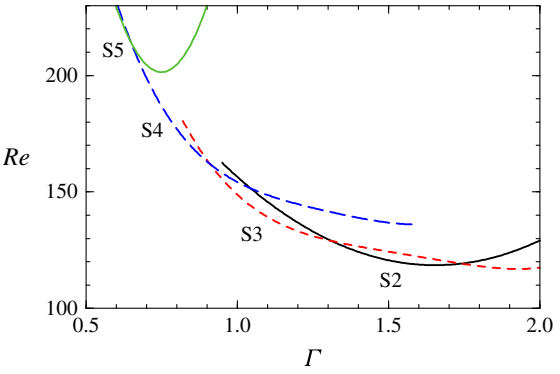


FIGURE 4. (Colour online) Loci in (Γ, Re) parameter space of circle-pitchfork bifurcations where BS loses stability to $\mathcal{H}$-symmetric steady states Sm, with azimuthal wavenumber m as indicated, upon crossing from low values of Re and Γ.

resulting in two meridional recirculation cells indicated by the streamlines. The flow in each half-cylinder would be in solid-body rotation (constant angular velocity), with opposing senses, if not for the presence of the flow in the other half-cylinder. These two counter-rotating bodies of fluid meet at the mid-plane $z = 0$ and the vortex lines cannot be aligned with the axis at the mid-plane. The vortex lines emerge from the rotating endwalls and bend to be parallel to the mid-plane as they approach the split in the cylinder sidewall for the symmetric BS flow state. This vortex line bending produces the mid-plane shear layer and drives the meridional circulation, characterized by the streamlines in each cylinder half where flow is driven radially in toward the axis from the split in the sidewall along $z = 0$. By approximately mid-radius, the meridional flows turn toward the respective endwalls at $z = \pm 0.5\Gamma$. The meridional flows in the endwall boundary layers are toward the sidewall. In the sidewall layer, the meridional flow is returned to the vicinity of the split at $z = 0$, completing the meridional circulation. A consequence of the meridional flows in the two halves is that the interior flows rotate slower than the respective endwalls, as evidenced from the angular velocity plot.

For comparison purposes, the corresponding plots for BS in the von Kármán swirling flow at the same (Γ, Re) are shown in the bottom row of figure 3. The vortex lines still emerge from the rotating endwalls, but due to the sidewall being stationary, they terminate at the corners where the sidewall and the endwalls meet. This results in the azimuthal shear at the mid-plane, $\partial v/\partial z|_{z=0}$, being much weaker than in the split-cylinder case, and the angular velocity in the interior is also considerably weaker. The resultant meridional flow is strongest near the corners where the vortex lines terminate, in contrast to the split sidewall case where the meridional flow is strongest near the sidewall split, which is where its vortex lines terminate. All in all, the split sidewall case produces a more intense azimuthal shear layer at mid-height with a stronger meridional jet flow at mid-height.

3.2. *Circle-pitchfork bifurcations to steady $\mathcal{H}$-symmetric states* Sm

For small enough Re, depending on Γ, the steady $O(2)$-symmetric BS flow is stable. Over the range of aspect ratios considered, $\Gamma \in [0.5, 2.0]$, the basic state BS loses stability as Re is increased via circle-pitchfork bifurcations where the flow loses axisymmetry (the $\mathcal{R}_\alpha$ invariance is broken), but remains steady ($\mathcal{T}_\beta$ invariant). Figure 4

https://doi.org/10.1017/jfm.2017.103 Published online by Cambridge University Press

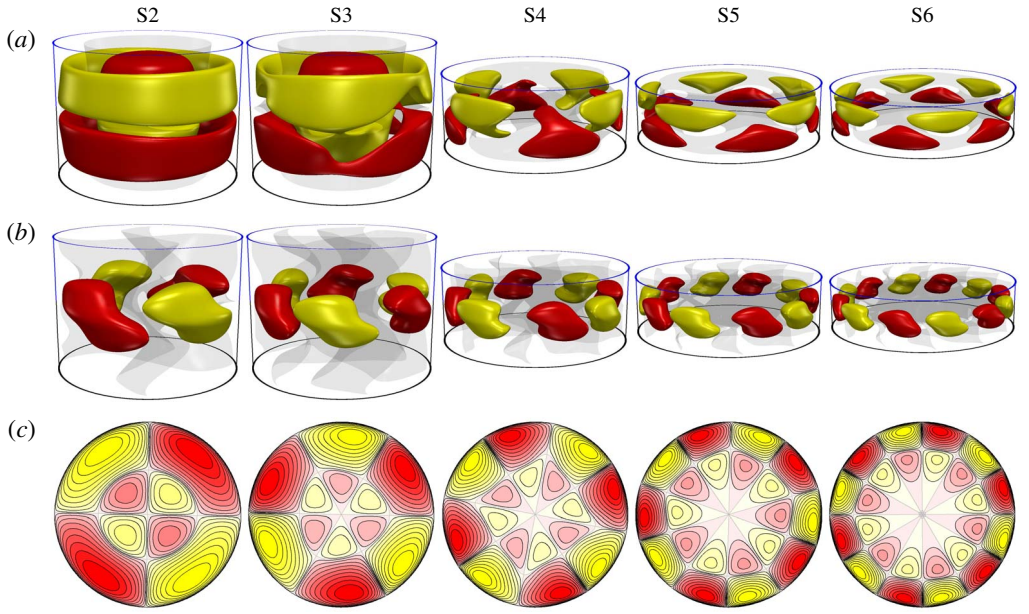


FIGURE 5. (Colour online) Isosurfaces of w (a), w–w_0 (b) and contours of w at $z=0$ (c), for S2 at $(\Gamma, Re) = (1.45, 123)$, S3 at $(\Gamma, Re) = (1.45, 135)$, S4 at $(\Gamma, Re) = (0.80, 225)$, S5 at $(\Gamma, Re) = (0.60, 250)$ and S6 at $(\Gamma, Re) = (0.50, 300)$.

shows the loci of the various circle-pitchfork bifurcations in (Γ, Re) parameter space. Although the continuous invariance $\mathcal{R}_\alpha$ (with α any angle) is broken, the flow retains a discrete invariance $\mathcal{R}_{2\pi/m}$, where m is the dominant azimuthal wavenumber of the flow. The value of m depends on Γ. We shall refer to these steady flows as Sm. Figure 5 shows typical Sm states, with $m \in [2, 6]$, where for each case, isosurfaces of the axial velocity w, and of the non-axisymmetric component w–w_0, where w_0 is the azimuthal average of w, are shown, together with contours of w at the mid-plane $z=0$ (note that for these steady states, $w_0 = 0$ at $z=0$). The isosurface levels depicted in this and in subsequent figures are all at ± 0.4 of the maximum of w and w–w_0, respectively. The contour levels of w at the mid-plane are quadratically spaced in $\pm \max(w|_{z=0})$, to enable comparisons between solutions at different points in (Γ, Re) parameter space. The bifurcating states Sm are $\mathcal{H}_\gamma$ invariant, but instead of γ being any angle, now there are only $2m$ angles differing by multiples of π/m for which the states are $\mathcal{H}$-symmetric. The angles are easily identified, they correspond to the orientations of the straight lines, along which $w = 0$, through the origin the cylinder mid-plane (see figure 5). For any m, there is a group orbit of stationary $\mathcal{H}$-symmetric states Sm with azimuthal wavenumber m. All members of the group are obtained from any one of them by rotating it in azimuth, giving a whole circle of solutions. Which one is realized depends on initial conditions.

In summary the Sm have the invariances $\mathcal{R}_{2\pi/m}\boldsymbol{u} = \boldsymbol{u}$, $\mathcal{H}_\gamma \boldsymbol{u} = \boldsymbol{u}$ for $2m$ angles differing by multiples of π/m, and $\mathcal{T}_\beta \boldsymbol{u} = \boldsymbol{u}$ for arbitrary β.

For the von Kármán swirling flow, it has been suggested that the shear layer at mid-height in the basic state loses stability via a Kelvin–Helmholtz type of instability leading to steady states with azimuthal wavenumbers $m \approx 2/\Gamma$ (Nore *et al.* 2003, 2004). In our flow, we do not find strong evidence for this. Figure 4 shows that S2

https://doi.org/10.1017/jfm.2017.103 Published online by Cambridge University Press

bifurcates for $\Gamma \sim 1.5$, and S3 bifurcates for both $\Gamma \sim 1$ and $\Gamma \sim 2$, and both co-exist over a large range of Γ. Another mechanism that is acting to make BS unstable is the counter rotation. Vortex lines in a rotating system have a tendency to align with the rotation axis. When the flow is axisymmetric, the exact counter rotation of the two halves of the cylinder results in the vortex lines being forced to be tangential to the mid-plane. By breaking axisymmetry, some of the vortex lines from one half can penetrate partially into the other half, resulting in the interface between the two counter-rotating bodies of fluid being undulated. The axial velocity w at $z = 0$ is a proxy for the interface undulation; this is shown in the third row of figure 5 for the different Sm found. Furthermore, for the Kelvin–Helmholtz instability of shear flow in a constant density fluid, the base flow velocity vector is planar two-dimensional and the vorticity vector is orthogonal to the velocity (i.e. the helicity, dot product of the velocity and vorticity vectors, is zero). In the problem under study, where the shear layer is due to counter-rotating bodies of fluid, the flow has non-zero helicity even in the absence of any instability, and the helicity is more intense when axisymmetry is broken. Large values of helicity indicate that the velocity and vorticity vectors are more aligned, and this leads to intensification of the vorticity via vortex stretching. Viscous dissipation can limit this process. In a related flow, consisting of a rotating cylinder with a counter-rotating top endwall (Lopez *et al.* 2002), a shear layer emanating from the corner where the sidewall and the counter-rotating top meet separates the counter-rotating bodies of fluid. That flow loses axisymmetry at Re approximately an order of magnitude larger than in the present split-cylinder arrangement. The instability is also associated with the vortex lines trying to align themselves with the rotation axis and in doing so they try to penetrate through the shear layer. With the larger Re, this penetration is not as viscously damped, and the result is a number of funnels of counter-rotating fluid, intensified by vortex stretching, penetrating all the way to the opposite endwall boundary layer. This type of behaviour is also present in the split-cylinder problem, but the penetration is symmetric into both halves, and not as intense due to the viscous dissipation in the lower Re flow.

The bifurcation curves in figure 4 indicate that there are several codim-2 points where two different circle-pitchfork bifurcation curves intersect. As is typical in many problems with $O(2)$ symmetry, these codim-2 points correspond to curves with wavenumbers m and $m + 1$. These points organize the mode interaction dynamics. Dangelmayr (1986) has shown that these mode interactions lead to rather distinct behaviour depending on if $m = 1$ or $m > 1$. The case $m = 1$ gives rise to the $1:2$ resonant interaction, which has attracted much theoretical interest and was found and studied in the von Kármán swirling flow by Nore *et al.* (2003). In our flow for the range of Γ considered, there is no circle-pitchfork bifurcation with $m = 1$. However, for $\Gamma \in (1.3, 1.75)$, a circle-pitchfork bifurcation with $m = 2$ is flanked by two others with $m = 3$, and Dangelmayr (1986) showed that the $2:3$ mode interaction also has distinct behaviour compared to mode interactions with higher wavenumbers.

3.3. *The 2 : 3 mode interaction*

Figure 6 shows the circle-pitchfork bifurcation curves along which S2 and S3 bifurcate from BS together with schematics of phase portraits in distinct regions in the neighbourhood of the codim-2 point where S2 and S3 bifurcate simultaneously. Generically, these circle-pitchfork bifurcation curves either do not intersect or they intersect at two points (Dangelmayr 1986; Higuera, Riecke & Silber 2004). In figure 6, there are two such intersection points, $(\Gamma, Re) = (1.3, 129.5)$ and $(1.78, 118.7)$. We

https://doi.org/10.1017/jfm.2017.103 Published online by Cambridge University Press

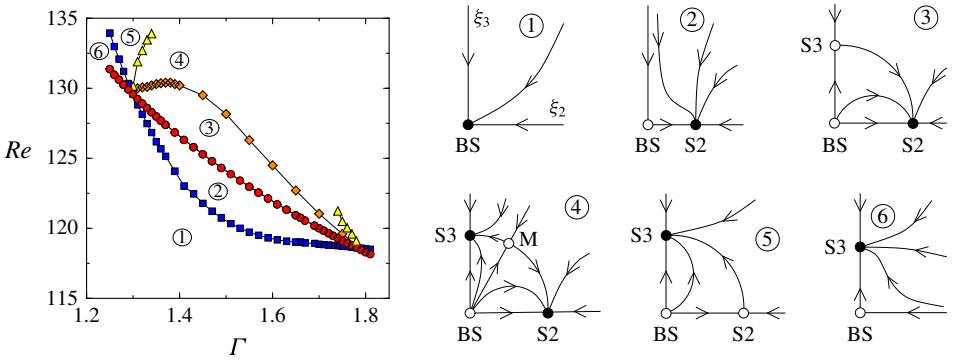


FIGURE 6. (Colour online) Bifurcation curves near the 2 : 3 mode interaction, together with schematic phase portraits in the regions near the codim-2 point at $(\Gamma, Re) = (1.3, 129.5)$; ξ_2 and ξ_3 are the $m = 2$ and $m = 3$ subspaces.

now consider a circular parameter sweep around one of these codim-2 points. In region 1, BS is the unique solution and it is stable. On increasing *Re*, BS loses stability to either S2 or S3, depending on Γ. S2 and S3 belong to the subspaces ξ_2 and ξ_3, respectively. Crossing from region 1 to region 2, the circle-pitchfork bifurcation renders BS unstable, and a stable group of S2 emerges. There are no other equilibria, stable or unstable, in region 2. Crossing into region 3 from region 2, BS undergoes another circle-pitchfork bifurcation and a group of S3 emerges and are unstable. Crossing from region 3 to region 4, S3 undergoes a steady-state bifurcation where it becomes stable. The normal form theory (see Dangelmayr 1986; Higuera *et al.* 2004, for more details) says that two types of unstable mixed modes are spawned at the bifurcation (which we simply call M in the figure). These mixed modes have non-zero $m = 2$ and $m = 3$ azimuthal Fourier components. Since the mixed modes M are unstable and they do not reside in either the ξ_2 or ξ_3 subspace and they are not directly detectable.

Crossing from region 4 into region 5, another steady-state bifurcation takes place rendering S2 unstable (by absorbing the unstable mixed mode M). Crossing from region 5 to region 6, S2 is absorbed into BS at the circle-pitchfork bifurcation. In region 6, the only equilibria are the stable S3 and unstable BS. Crossing from region 6 back to region 1 completes the parameter sweep around the codim-2 point, and S3 is absorbed into BS at the circle-pitchfork bifurcation where BS regains stability. The two circle-pitchfork bifurcations where S2 and S3 bifurcate from BS were found by direct simulations in the ξ_2 and ξ_3 subspaces, respectively. The steady-state bifurcations where S2 and S3 change stability were found by simulations in the full space ξ_1.

3.4. *Parameter sweep in Re with* $\Gamma = 1.45$

In order to investigate the nonlinear dynamics beyond the circle-pitchfork bifurcations, we focus on varying *Re* while keeping $\Gamma = 1.45$ fixed, which provides a parameter sweep through the middle of the region organized by the pair of 2 : 3 codim-2 points shown in figure 6. Figure 7 provides a summary of the various states and their stability in terms of the modal energy in their primary azimuthal wave number. Filled symbols indicate stable states in the full space ξ_1 and open symbols indicate unstable states which were computed in their respective subspaces ξ_m.

https://doi.org/10.1017/jfm.2017.103 Published online by Cambridge University Press

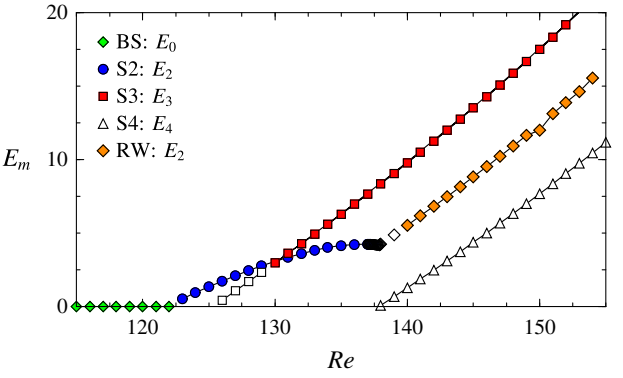


FIGURE 7. (Colour online) Variation of modal kinetic energies with Re for various states as indicated, with $\Gamma = 1.45$. The unstable states (open symbols) were computed in their respective subspaces.

With $\Gamma = 1.45$ fixed, BS is stable for $Re \lesssim 122.5$. It becomes unstable for larger Re via the circle-pitchfork spawning the circle of steady states S2. At $Re \approx 125.5$, BS undergoes another circle-pitchfork bifurcation and spawns a circle of steady states S3, which are unstable since BS is also unstable. This bifurcation and the unstable S3 were computed in the subspace ξ_3. At $Re \approx 129.5$, the unstable S3 undergoes a bifurcation at which it is rendered stable. So far, all of these bifurcations were discussed in the context of figure 6, and are associated with the dynamics local to the 2 : 3 codim-2 points. As Re approaches 138, a number of other events unfold. At $Re \approx 137.5$, S2 becomes unstable. At slightly larger Re, using S2 from slightly lower Re as the initial condition, the flow evolves to the stable S3. However, restricting the flow to the ξ_2 subspace, S2 remains stable until $Re \approx 137.9$, at which point it loses stability via a drift-pitchfork bifurcation (Coullet & Iooss 1990; Crawford & Knobloch 1991; Fauve, Douady & Thual 1991; Kness, Tuckerman & Barkley 1992) at which a rotating wave, RW, with azimuthal wavenumber $m = 2$ is spawned. This RW will be described in detail in § 3.5. S2 continues to exist beyond the drift-pitchfork bifurcation but it is unstable, both in ξ_1 and ξ_2, and we do not have a convenient way to compute it.

Also at $Re \approx 137.9$, BS undergoes a third circle-pitchfork bifurcation creating an unstable S4 which we are able to compute in the ξ_4 subspace. We have continued the S4 branch in ξ_4 to $Re = 200$. Note that S2 and S3 do not exist in ξ_4. In ξ_4, S4 is stable until it loses stability at $Re \approx 161.5$ in a supercritical Hopf bifurcation that breaks the $\mathcal{H}_\gamma$ symmetry of S4, spawning a direction-reversing wave (Landsberg & Knobloch 1991). This DRW will be described in detail in § 3.6.

3.5. *Rotating wave RW from a drift-pitchfork bifurcation*

As mentioned above, the drift-pitchfork bifurcation takes place in ξ_2 as S2 is unstable in the full space ξ_1. A distinct characteristic of the drift-pitchfork bifurcation is that it breaks the $\mathcal{H}_\gamma$ symmetry. Like the S2 from which they bifurcate, RW have broken rotational invariance $\mathcal{R}_\alpha$ (for arbitrary α, except $\alpha = \pi$), and since $\mathcal{H}_\gamma$ is also broken, they drift slowly in θ near onset. Since the $\mathcal{H}_\gamma$ symmetry is broken, these rotating waves come in counter-rotating pairs; one is obtained by applying $\mathcal{H}_\gamma$ to the other, and which one is realized depends on initial conditions. The drift speed is zero at the bifurcation at $Re = Re_c$, and it grows as $\sqrt{|Re - Re_c|}$. A typical RW at $(\Gamma, Re) =$

https://doi.org/10.1017/jfm.2017.103 Published online by Cambridge University Press

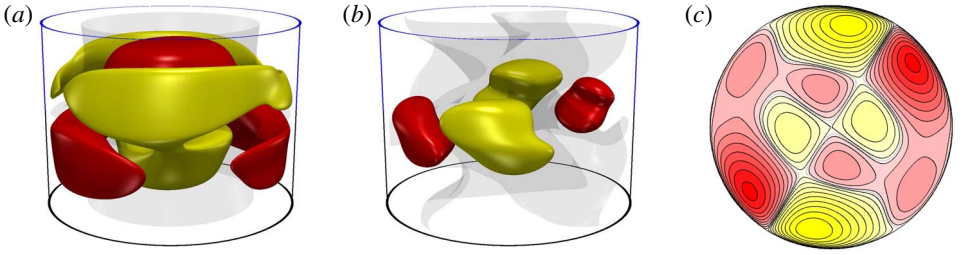


FIGURE 8. (Colour online) Isosurfaces of (*a*) w, (*b*) w–w_0 and (*c*) contours of w at $z = 0$, for RW at $(\Gamma, Re) = (1.45, 142)$. See the online movie 1 available at https://doi.org/10.1017/jfm.2017.103 for an animation of w–w_0.

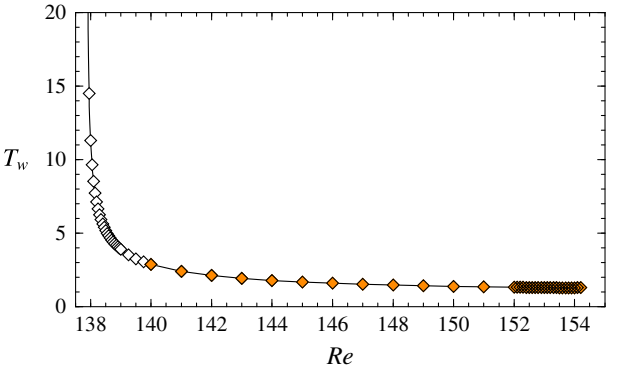


FIGURE 9. (Colour online) Drift period of RW, T_w, versus Re, together with a curve fit $T_w = 0.117 + 4.018/\sqrt{Re - 137.872}$. The unstable RW (open symbols) were computed in ξ_2.

(1.45, 142) is shown in figure 8. The broken $\mathcal{H}_\gamma$ symmetry is most clearly detected in the contour plot of w at the mid-plane, which has no straight $w = 0$ contour through the centre of the cylinder (compare with the $w(z = 0)$ contour plot for S2 in figure 5, which has two such lines through the centre).

Since rotating waves simply drift at a constant speed without change of shape (see the associated online movie 1), their modal kinetic energies are time invariant, but a point-wise measure (a velocity component at some point) has a periodic signal. The period of such a signal, T_w, for RW as a function of Re is shown in figure 9. The open symbols correspond to RW computed in ξ_2 and the filled symbols correspond to RW computed in the full space ξ_1. The curve fit is $T_w = 0.117 + 4.018/\sqrt{Re - 137.872}$, indicating that the drift-pitchfork bifurcation happens at $Re \approx 137.872$. In summary, the RW have the invariances $\mathcal{R}_\pi \boldsymbol{u} = \boldsymbol{u}$, $\mathcal{R}_\alpha \boldsymbol{u} = \mathcal{T}_{(\alpha T_w)/2\pi} \boldsymbol{u}$ for arbitrary α, and $\mathcal{T}_{T_w} \boldsymbol{u} = \boldsymbol{u}$.

At $Re \approx 139.8$, the unstable RW undergoes a bifurcation in ξ_1 that renders it stable for larger Re. What is spawned at this bifurcation is unstable and we do not have any direct information to determine its features, but the bifurcation must be of subcritical symmetry-breaking type as RW in ξ_2 does not change stability type in this range of Re. RW remains stable up to $Re \approx 154.1$; simulations at slightly larger Re using RW at slightly lower Re as the initial condition evolve to a different time-dependent state that has very different spatio-temporal characteristics compared to RW. We call this new state a pulse wave PWs, for reasons that will become evident when we describe it in § 3.7.

https://doi.org/10.1017/jfm.2017.103 Published online by Cambridge University Press

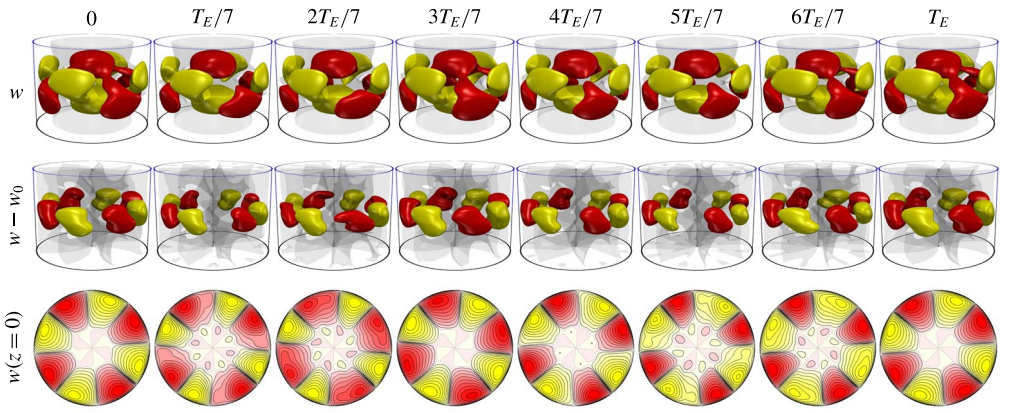


FIGURE 10. (Colour online) Snapshots over one T_E period relative to an arbitrary reference time of w-isosurfaces, w–w_0-isosurfaces and w contours at $z = 0$ for DRW at $(\Gamma, Re) = (1.45, 165)$ computed in ξ_4. See the online movie 2 for an animation of w–w_0.

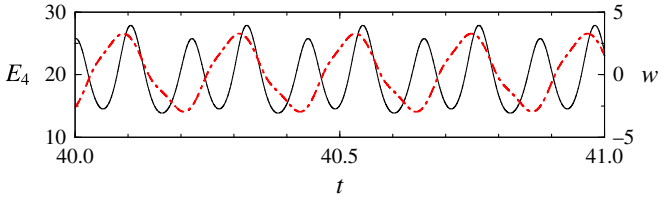


FIGURE 11. (Colour online) Time series of E_4 (solid line) and $w(0.98, 0, -0.4\Gamma)$ (dashed line) of DRW at $(\Gamma, Re) = (1.45, 165)$, computed in ξ_4.

3.6. *Direction-reversing wave from a Hopf bifurcation*

We now turn our attention to ξ_4 and S4 that bifurcates from BS at $Re \approx 137.9$. S4 loses stability in ξ_4 at $Re \approx 161.5$ in a supercritical Hopf bifurcation that breaks the $\mathcal{H}_\gamma$ symmetry. Figure 10 shows snap-shots over one period of the direction-reversing wave DRW at $(\Gamma, Re) = (1.45, 165)$, and the accompanying movie 2 animates the w–w_0 isosurfaces for this case, illustrating how the structure oscillates back and forth in the azimuthal direction with a swelling and deflation of the structure in a period T_E (the period of the modal kinetic energy variation). The key ingredient necessary for a direction-reversing wave is a Hopf bifurcation that breaks the reflection symmetry of a circle of non-trivial steady states, in our case these are S4 (Landsberg & Knobloch 1991). The breaking of the $\mathcal{H}_\gamma$ symmetry is most clearly seen by comparing the $w(z = 0)$ contour plots of DRW in figure 10 with those of S4 in figure 5, which is $\mathcal{H}$-symmetric about four lines through the axis.

Unlike RW which have constant modal kinetic energies, the modal kinetic energies of DRW are time periodic. Their frequency is associated with the Hopf frequency at the bifurcation and the peak-to-peak amplitude in the modal kinetic energies grow linearly from zero with $|Re - Re_c|$, for $Re \sim Re_c$. Figure 11 shows time series of modal kinetic energy E_4 and of $w(0.98, 0, -0.4\Gamma)$ for DRW at $(\Gamma, Re) = (1.45, 165)$; both are periodic with period T_E. Figure 12 shows the variations with Re of the peak-to-peak amplitude and period of E_4 for DRW. Near the bifurcation at $Re \approx 161.5$, the behaviour of the amplitude and period is typical of a supercritical Hopf bifurcation

https://doi.org/10.1017/jfm.2017.103 Published online by Cambridge University Press

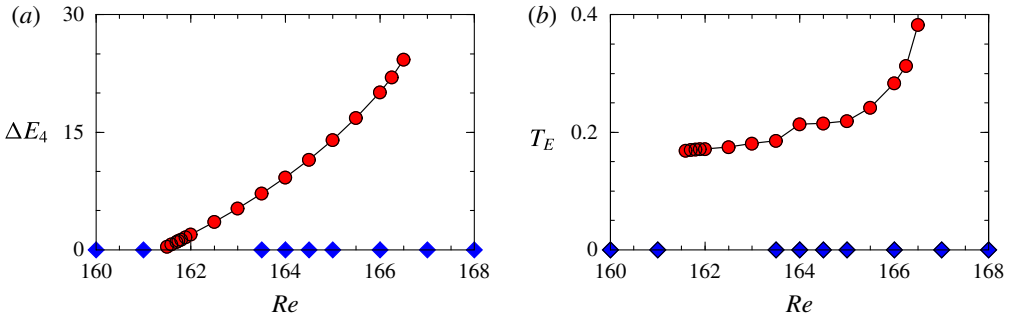


FIGURE 12. (Colour online) (*a*) Peak-to-peak amplitude and (*b*) period of E_4 for DRW at $\Gamma = 1.45$, computed in ξ_4. The stable S4 are indicated as (blue) diamonds in order to show the region of hysteresis between S4 and DRW.

(Strogratz 1994). DRW loses stability at $Re \approx 166.5$ in what is most likely a cyclic-fold bifurcation (saddle-node bifurcation of limit cycles), and S4 is stable for larger Re. We have continued S4 in ξ_4 up to $Re = 200$. Also, we have continued S4 to lower Re, and find that it becomes unstable at $Re \approx 163.5$ where is undergoes a subcritical Hopf spawning an unstable DRW to higher Re which is involved in the cyclic-fold bifurcation at $Re \approx 166.5$.

The fundamental difference between RW and DRW is that while both result from bifurcations of Sm that break $\mathcal{H}_\gamma$ (S2 for RW and S4 for DRW), the bifurcation leading to RW is steady (real eigenvalue crosses zero) while that leading to DRW is not (the real part of a complex-conjugate pair of eigenvalues changes sign), so for RW the phase change is constant whereas for DRW it is periodic (Landsberg & Knobloch 1991). In summary, the DRW have the invariances $\mathcal{R}_{\pi/2}\boldsymbol{u} = \boldsymbol{u}$ and $\mathcal{T}_{T_E}\boldsymbol{u} = \boldsymbol{u}$.

3.7. *Pulse waves*

Attempts to continue RW beyond $Re \approx 154.1$ in ξ_2 result in the same evolutions as in ξ_1, indicating that RW ceases to exist beyond $Re \approx 154.1$ due to a cyclic-fold bifurcation. For Re beyond this bifurcation, we find pulse wave states PWs. Like RW, PWs are invariant to $\mathcal{R}_\pi$, i.e. they reside in ξ_2. The PWs are stable to lower $Re \approx 153.3$, below which they are destroyed, presumably also in a cyclic-fold bifurcation, so that we have a region of hysteresis between RW and PWs over $Re \in (153.3, 154.1)$.

Figure 13(*a*) shows the time-averaged modal kinetic energy $\langle E_2 \rangle$ for RW and PWs over their hysteresis region in Re. Note that $\langle E_2 \rangle = E_2$ for RW. Figure 13(*b*) shows the corresponding energy period, T_E, of oscillation in E_2. For RW, $T_E = 0$ since the solution is only rotating, uniformly changing its azimuthal orientation, but not changing its structure.

PWs is an unsteady flow with slow–fast dynamics, as can be seen from the time series of E_2 and E_4 shown in figure 14(*a*). The fast dynamics consists of a rapid growth in E_2; when E_2 reaches its maximum, E_4 begins to grow and E_2 slowly decays, then the cycle repeats. The dynamics is easiest to visualize from isosurfaces of w–w_0. Figure 15 for PWs at $Re = 153.5$ shows snap-shots of w and w–w_0 isosurfaces and w contours at the mid-plane over one T_E period (the associated online movie 3 animates the w–w_0 isosurfaces over $8T_E$ to better illustrate the slow–fast dynamics). The steady state S2 has two pairs of oppositely signed blobs of w–w_0 symmetrically distributed in azimuth about the mid-plane. In the slow phase of PWs, there are

https://doi.org/10.1017/jfm.2017.103 Published online by Cambridge University Press

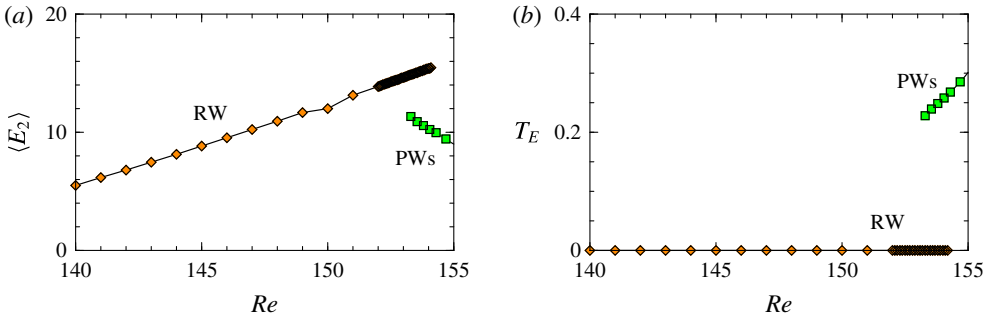


FIGURE 13. (Colour online) Variation with Re of (a) the time-averaged modal energy $\langle E_2 \rangle$ and (b) the period T_E of RW and PWs, for $\Gamma = 1.45$, computed in the full space ξ_1.

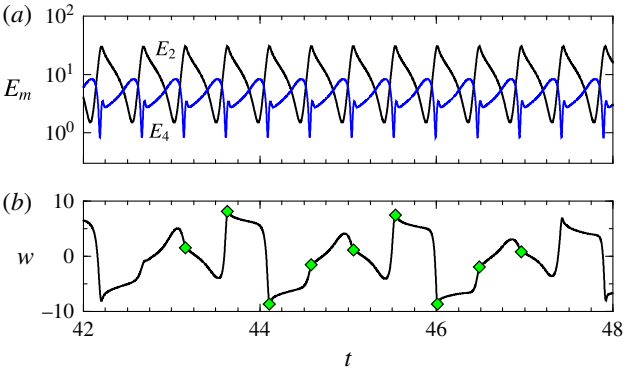


FIGURE 14. (Colour online) Time series of (a) modal kinetic energies E_2 and E_4, and (b) $w(0.98, 0, -0.4\Gamma)$ for PWs at $(\Gamma, Re) = (1.45, 153.5)$. The (green) diamonds correspond to the numbered diamonds in figure 16.

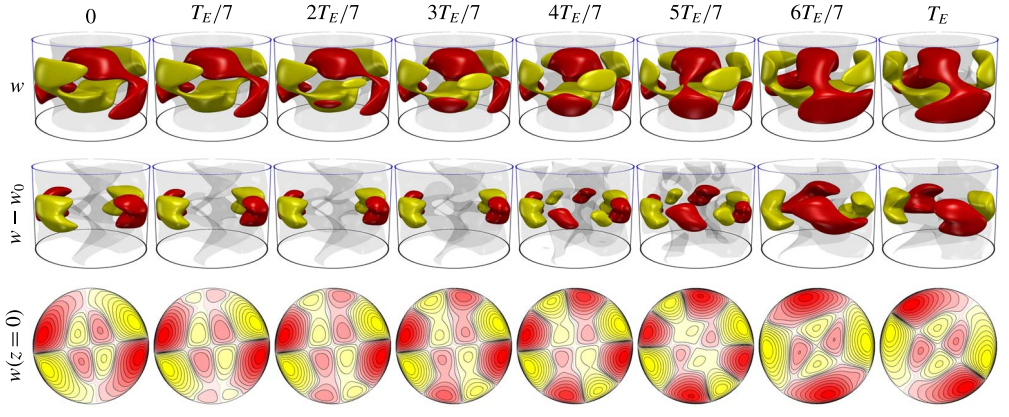


FIGURE 15. (Colour online) Snapshots over one T_E period relative to an arbitrary reference time of w-isosurfaces, w–w_0-isosurfaces and w contours at $z = 0$ for PWs at $(\Gamma, Re) = (1.45, 153.5)$. See the online movie 3 for an animation of w–w_0.

https://doi.org/10.1017/jfm.2017.103 Published online by Cambridge University Press

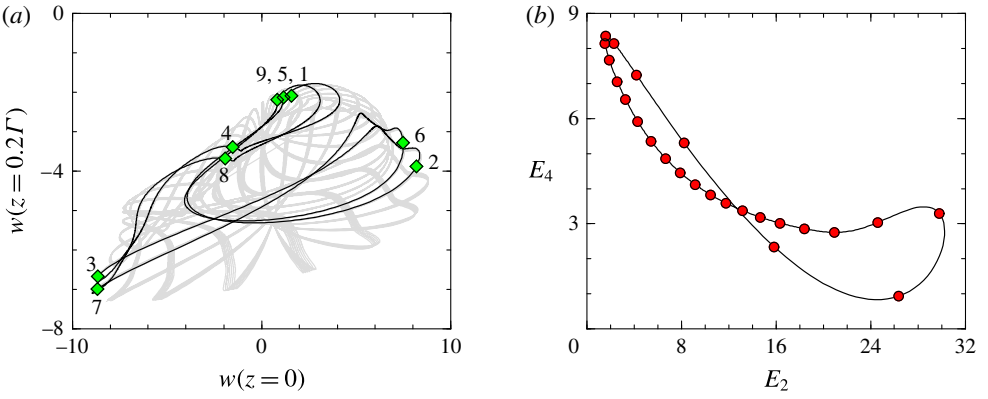


FIGURE 16. (Colour online) Phase portraits, (*a*) using $w(0.98,\ 0,\ 0,\ t)$ and $w(0.98,\ 0,\ 0.2\Gamma,\ t)$ and (*b*) using E_2 and E_4, for PWs at $(\Gamma,\ Re) = (1.45,\ 153.5)$; there are 25 equispaced-in-time circular markers over T_E.

also two pairs of oppositely signed blobs of w–w_0. These blobs slowly diminish in size and the oppositely signed blobs in each pair slowly approach each other. In so doing, two increasingly wide swaths with near-zero w–w_0 result about the mid-plane. Then, during the fast phase of the oscillation, two new pairs of blobs appear in the near-zero swaths between the two existing pairs. When the new blobs are comparable to the pre-existing blobs, the positive new blobs and the negative old blobs move toward each other and the other blobs vanish, leaving a configuration that again closely resembles the S2 steady state, but rotated by approximately $\pi/4$ with respect to the earlier orientation. This occurs in one period T_E and the original orientation is almost regained in about $8T_E$.

Although the time series of the modal kinetic energies of PWs are T_E-periodic, PWs are not time periodic. This is evident from the time series of $w(0.98,\ 0,\ -0.4\Gamma)$, shown in figure 14(*b*); the (green) diamonds in the figure are equispaced every T_E and correspond to maxima in E_2. What happens is that in exactly one period T_E, the structure of PWs is the same as its structure a period earlier, and hence has the same modal kinetic energies, but its orientation has changed by almost $\pi/4$, and so the local measure of w is different. If the orientation had changed by exactly $\pi/4$ (or some other rational fraction of π), the w signal would also be periodic, but this does not happen generically. Figure 16(*a*) shows a phase portrait of PWs at $(\Gamma, Re) = (1.45,\ 153.5)$, using $w(0.98,\ 0,\ 0)$ and $w(0.98,\ 0,\ 0.2\Gamma)$, over many T_E, showing the structure of a 2-torus in grey. The line in black is a part of the trajectory over $8T_E$ and the (green) diamonds correspond to the same symbols in the corresponding time series in figure 14. The trajectory is almost a cycle that closes in on itself. However, it does not; the symbol labelled 9 does not coincide with that labelled 1, and the trajectory eventually covers the torus. Such states are sometimes referred to as relative periodic orbits, states that would appear to be periodic if viewed from a reference frame rotating at the angular rate corresponding to the angular change in orientation every T_E period. This is in the same sense that rotating waves are relative equilibria, states that would appear steady when viewed from a reference frame rotating at the angular rotation rate of the rotating wave. In figure 16(*b*), a phase portrait of the same PWs is shown using E_2 and E_4. This is a closed cycle, as expected. The symbols on the closed curve correspond to 25 uniformly spaced times over T_E, to show the slow–fast character of the oscillation.

https://doi.org/10.1017/jfm.2017.103 Published online by Cambridge University Press

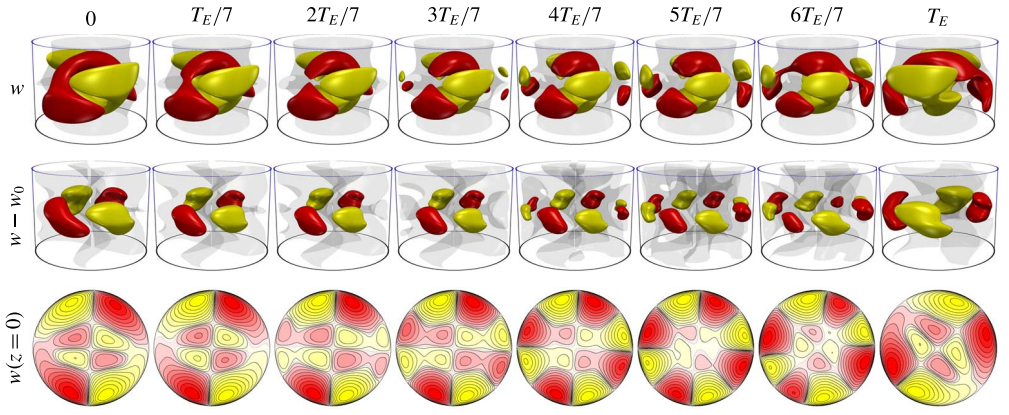


FIGURE 17. (Colour online) Snapshots over one T_E period relative to an arbitrary reference time of w-isosurfaces, w–w_0-isosurfaces and w contours at $z = 0$ for PWa at $(\Gamma, Re) = (1.45, 160)$ computed in ξ_2. See the online movie 4 for an animation of w–w_0.

In summary, the PWs have the invariances $\mathcal{R}_\pi \boldsymbol{u} = \boldsymbol{u}$ and $\mathcal{R}_\alpha \boldsymbol{u} = \mathcal{T}_{T_E} \boldsymbol{u}$ for some α that is not a rational fraction of π.

3.8. *Symmetry breaking to PWa*

The pulse wave PWs is stable in ξ_1, but resides in ξ_2 since all of its odd azimuthal Fourier components have zero modal kinetic energy. PWs is stable up to $Re \approx 155.15$, where it loses stability in a supercritical symmetry-breaking bifurcation breaking the $\mathcal{R}_\pi$ rotational invariance. The state that is spawned is referred to as PWa. The bifurcation results in the $m = 3$ Fourier component being excited, and so PWa resides in the full space ξ_1. Like PWs, PWa has slow–fast dynamics, and for the most part looks very much like PWs, spending most of the time very close to the ξ_2 subspace, with a quick excursion out of it when E_3 is large. Figure 17 shows snap-shots of w and w–w_0 isosurfaces and w contours at the mid-plane over one T_E period for PWa at $(\Gamma, Re) = (1.45, 160)$. They are not very different from the corresponding images for PWs shown in figure 15. The phase portraits of PWa in figure 18 are also qualitatively the same as those for PWs shown in figure 16. However, the time series of E_1, E_2, E_3, E_4 and w in figure 19 clearly show how E_3 comes into play in the slow–fast dynamics. E_1 is smaller than and slaved to E_3, and comes about via the nonlinear interaction between E_3 with E_2 and E_4. Note that the E_m time series are also strictly T_E periodic, as for PWs. For both PWs and PWa, in exactly one period T_E, their structure is the same as it was a period earlier, and hence they have the same modal kinetic energies as they did one period earlier, but their orientation has changed, by almost $\pi/4$. They are both relative periodic orbits.

The PWa have the invariance $\mathcal{R}_\alpha \boldsymbol{u} = \mathcal{T}_{T_E} \boldsymbol{u}$ for some α that is not a rational fraction of π.

3.9. *Saddle-node-on-an-invariant-circle bifurcation destroying PWa*

The period T_E of PWa does not vary very much from its onset following the symmetry-breaking instability of PWs at $Re \approx 155.15$ to $Re \approx 200$. As Re is increased beyond 200, T_E becomes increasing larger. Figure 20 shows how the amplitude

https://doi.org/10.1017/jfm.2017.103 Published online by Cambridge University Press

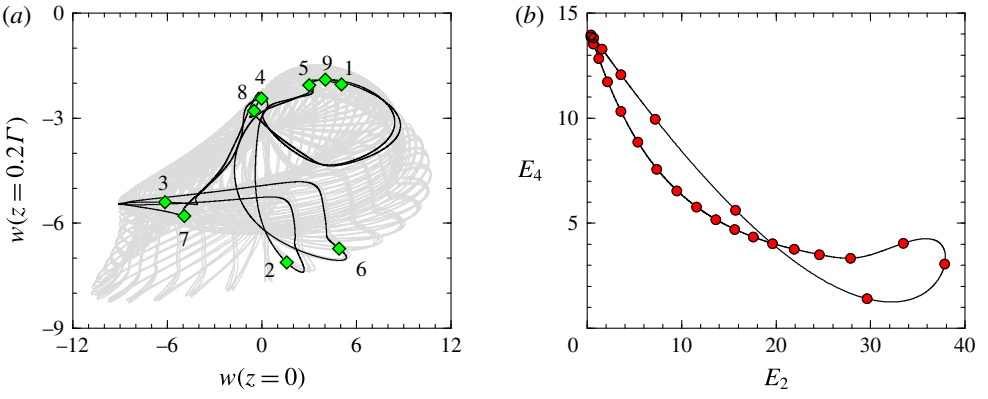


FIGURE 18. (Colour online) Phase portraits, (*a*) using $w(0.98,\ 0,\ 0,\ t)$ and $w(0.98,\ 0,\ 0.2\Gamma,\ t)$ and (*b*) using E_2 and E_4, for PWa at $(\Gamma,\ Re) = (1.45,\ 160)$; there are 25 equispaced-in-time circular markers over T_E.

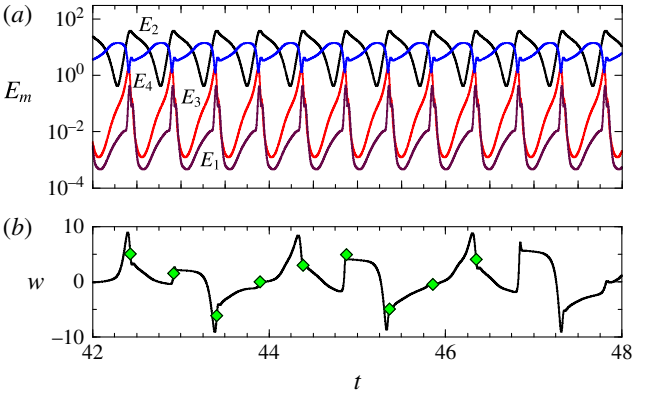


FIGURE 19. (Colour online) Time series of (*a*) modal kinetic energies E_1, E_2, E_3 and E_4 and (*b*) $w(0.98,\ 0,\ -0.4\Gamma)$ for PWa at $(\Gamma, Re) = (1.45,\ 160)$. The diamonds correspond to the numbered diamonds in figure 18.

(time-averaged E_2) and period T_E of RW, PWs and PWa vary with Re. Each symbol in the figure corresponds to an individual simulation that was run for many viscous times to establish its time-asymptotic behaviour. For $Re > 200$, these simulations have been run for between 100 and 200 viscous times in order to accurately estimate the period T_E. Over this Re range, $T_E = 0.285 + 0.831/\sqrt{206.312 - Re}$ is a very good fit to the computed period, and indicates that the period becomes unbounded at $Re = 206.312$.

This inverse-square-root behaviour of the period dependence on Re is typical of a SNIC bifurcation (a saddle-node-on-an-invariant-circle bifurcation). The slow–fast dynamics of PWa reaches a critical slowing down as $Re \to 206.312$. This is illustrated in figure 21, showing phase portraits of PWa at three Re approaching the critical value $Re = 206.312$. In the third portrait, corresponding to $Re = 206.30$, we find the (red) circles accumulate. On this same portrait we have included the $(E_2,\ E_4)$ point as a (green) diamond, corresponding to the stable steady state that is found following the SNIC bifurcation at $Re = 206.32$. This steady state is S2; its features are illustrated in

https://doi.org/10.1017/jfm.2017.103 Published online by Cambridge University Press

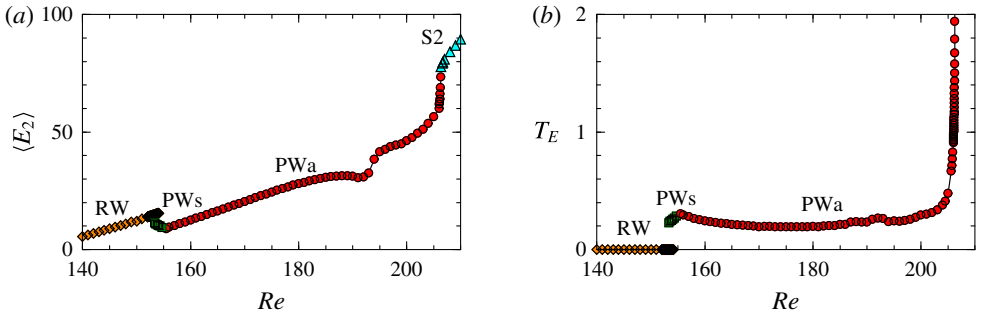


FIGURE 20. (Colour online) Variation with Re of (a) the time-averaged modal energy $\langle E_2 \rangle$ and (b) the period T_E of RW, PWs, PWa and S2 for $\Gamma = 1.45$, computed in the full space ξ_1. Near $Re = 206$, the period of PWa has the fit $T_E = 0.285 + 0.831/\sqrt{206.312 - Re}$.

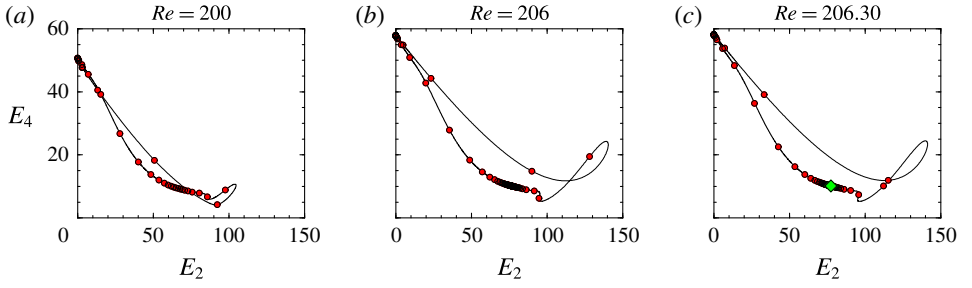


FIGURE 21. (Colour online) Phase portrait in (E_2, E_4) for PWa at $\Gamma = 1.45$ and Re as indicated. There are 25 equispaced-in-time circular markers over T_E, used to illustrate the slow–fast nonlinear oscillation. In (c), the (green) diamond corresponds to the steady S2 at $Re = 206.32$.

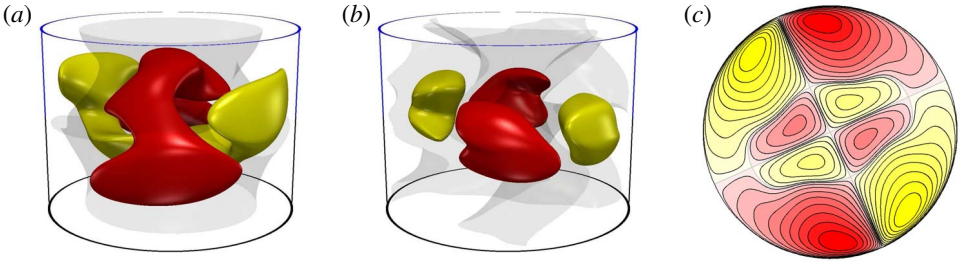


FIGURE 22. (Colour online) Isosurfaces of (a) w, (b) w–w_0 and (c) contours of w at $z = 0$, for S2 at $(\Gamma, Re) = (1.45, 206.32)$.

figure 22. It has the same features as PWa during it slow phase (e.g. compare with the 0 phase of figure 17).

3.10. *Behaviour over a broader range of parameter space*

The one parameter sweep varying Re while keeping $\Gamma = 1.45$ revealed very rich dynamics and multiplicity of solutions, all associated with the manner in which the $O(2)$ symmetry is broken. In this section, we provide a broader overview considering

https://doi.org/10.1017/jfm.2017.103 Published online by Cambridge University Press

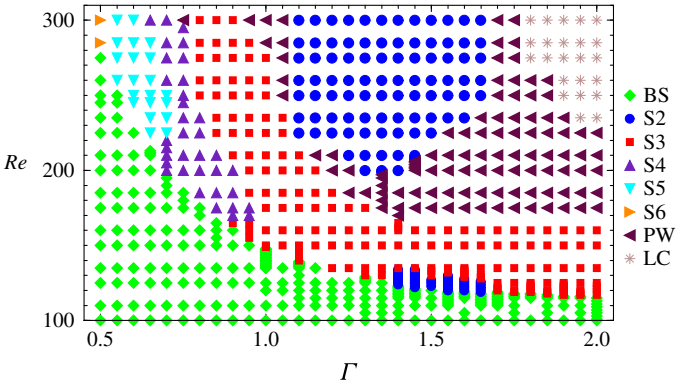


FIGURE 23. (Colour online) Loci of stable states in (Γ, Re), found by using BS at $Re = 100$ at each Γ as the initial condition for simulations for all Re at that Γ. No attempt was made to show loci of multiple stable states at the same point in parameter space that were found using other initial conditions.

variations in Γ as well, although not in anywhere near as much detail. We have considered $\Gamma \in [0.5, 2.0]$ in increments of 0.05, and used the BS at $Re = 100$ for each of these Γ as the initial conditions for larger Re. For each Γ, solutions with Re up to 300, in increments of about 10 were computed until transients died off (up to a few dozen viscous time units). Some refinements in Re were done near the bifurcations for some of the cases. Figure 23 is a summary of the states computed using that process (about 800 simulations). Very close to the primary circle-pitchfork bifurcation curves, the corresponding Sm states are obtained. However, not too far after the circle-pitchfork bifurcations, the steady state S3 is obtained over a wide swath of parameter space. Then, the parameter space is dominated either by various types of pulse wave states (PWs and PWa, as well as others to be described below), or the S2 state that was found following the destruction of PWa via the SNIC bifurcation. Also, for a parameter region with $\Gamma \sim 2$ and $Re \sim 300$, a limit cycle state without any non-trivial spatial symmetry (the invariance to $\mathcal{R}_{2\pi}$ is trivial), but with a space–time symmetry, exists (described below). Of course, there are multiplicities of solutions throughout the parameter space, and the manner in which we have solved the sequences of initial value problems does not bring any of that richness out (repeating the procedure used in the one parameter sweep at $\Gamma = 1.45$ for the 30 other values of Γ is beyond the scope of the present study). However, it does provide an indication of which solution types are likely to be found.

We now address, to a very small degree, the changes in the pulse waves for different aspect ratios. In the parameter sweep varying Re and keeping $\Gamma = 1.45$ fixed, the level to which E_3 grows for PWa remains relatively small. However, by varying Γ we have also found PWa in which E_3 is the dominant modal kinetic energy during a part of the oscillation. Figures 24 and 25 show snap-shots of w–w_0 isosurfaces and contour plots of w at the mid-plane, as well as time series of the modal kinetic energies and a phase portrait of PWa at $(\Gamma, Re) = (1.80, 175)$. While the PWa is of the same type as described earlier at $(\Gamma, Re) = (1.45, 160)$, it has a very different apparent dynamic due to E_3 being dominant over some time intervals. This is easiest to visualize from the online movie 5 showing w–w_0 isosurface.

Another different pulse wave, PWo, was found at $(\Gamma, Re) = (1.50, 210)$. It only has 2 plateaus of E_2 energy instead of the 8 plateaus of PWs and PWa. Figure 26 shows the

https://doi.org/10.1017/jfm.2017.103 Published online by Cambridge University Press

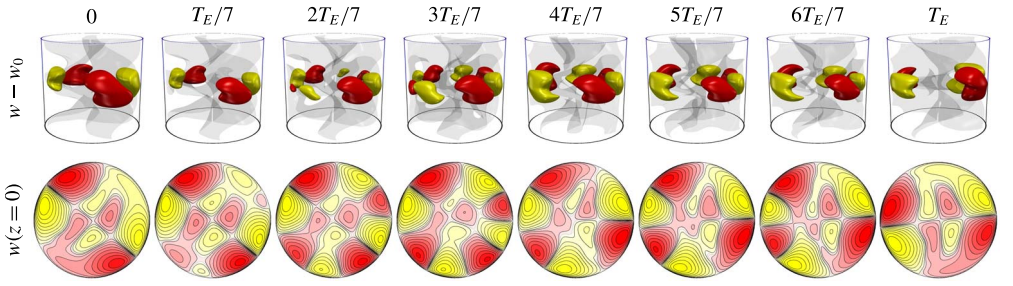


FIGURE 24. (Colour online) Snapshots over one T_E period, relative to an arbitrary reference time, of w–w_0-isosurfaces and w contours at $z = 0$ for PWa at $(\Gamma, Re) = (1.80, 175)$. See the online movie 5 for an animation of w–w_0.

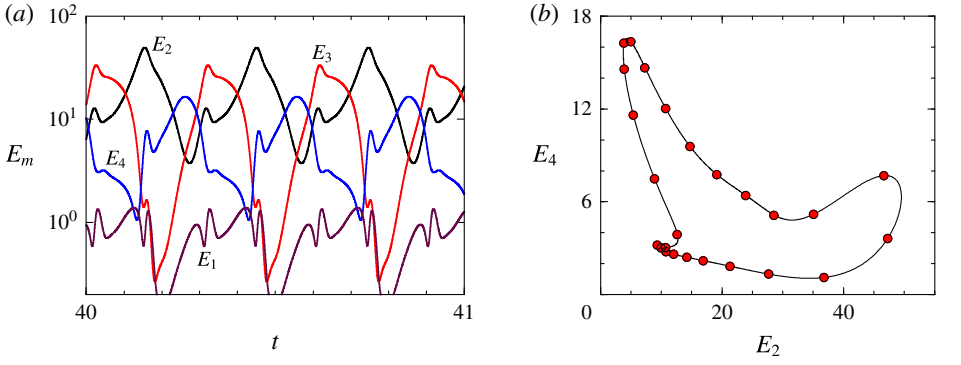


FIGURE 25. (Colour online) (*a*) Time series of E_m and (*b*) phase portrait using E_2 and E_4 for PWa at $(\Gamma, Re) = (1.80, 175)$.

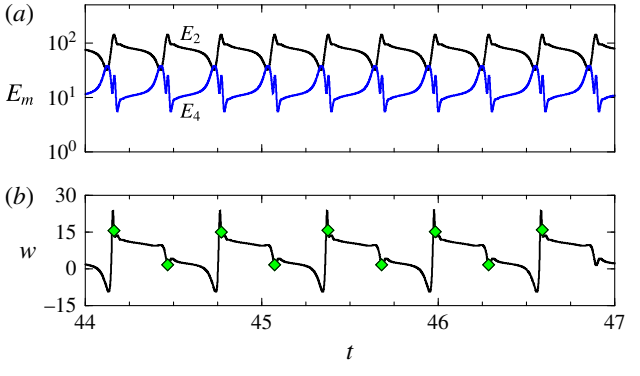


FIGURE 26. (Colour online) Time series of (*a*) modal kinetic energies E_2 and E_4 and (*b*) $w(0.98, 0, -0.4\Gamma)$ for PWo at $(\Gamma, Re) = (1.5, 210)$.

E_2 time evolution with the w evolution, showing that PWo is a periodic solution, with period $2T_E$, but the modal energies are T_E periodic. Figure 27 shows snapshots of w at the mid-plane together with isosurfaces of w–w_0. It pulses back and forth every $2T_E$, periodically switching its orientation, much like the DRW do. However, the oscillation

https://doi.org/10.1017/jfm.2017.103 Published online by Cambridge University Press

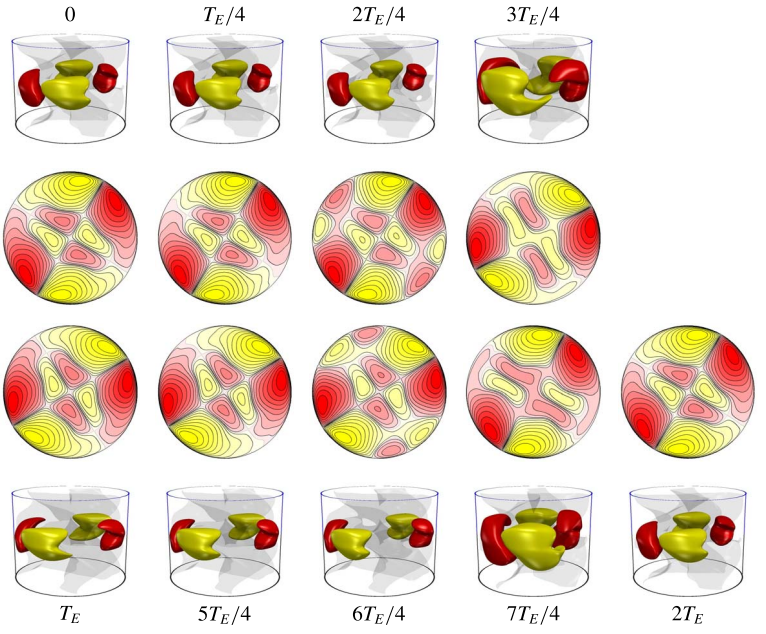


FIGURE 27. (Colour online) Snapshots of w–w_0 isosurfaces and w contours at $z=0$ over $2T_E$ relative to an arbitrary reference time for PWo at $(\Gamma, Re)=(1.50, 210)$. See the online movie 6 for an animation of isosurfaces of w–w_0.

is not smooth, but pulse-like. PWo have broken $\mathcal{R}_\alpha$ symmetry, for any angle α except π, so there is a group orbit of PWo obtained by applying $\mathcal{R}_\alpha$. Furthermore, since PWo have broken $\mathcal{H}_\gamma$ symmetry, there are two group orbits, one obtained by applying $\mathcal{H}_\gamma$ to the other (the angle γ is arbitrary, different values of γ will give a PWo on the other group orbit with a different orientation). PWo also have a space–time symmetry, a half-period-flip symmetry, where the flip is a composition of $\mathcal{H}_\gamma$ with a rotation. This half-period-flip symmetry can be seen by comparing the solution at some time t with the solution at $t+T_E$, particularly in the contours of w at the mid-plane as shown in figure 27.

In summary, the PWo has invariances $\mathcal{R}_\pi \boldsymbol{u}=\boldsymbol{u}$, $\mathcal{T}_{2T_E}\boldsymbol{u}=\boldsymbol{u}$, and $\mathcal{T}_{T_E}\boldsymbol{u}=\mathcal{R}_{\phi-2\gamma}\mathcal{H}_\gamma\boldsymbol{u}$ for γ arbitrary and a given ϕ.

In the upper ranges of parameter space investigated, with $\Gamma\sim 2$ and $Re\sim 300$ (indicated in the upper right corner of figure 23) we have encountered limit cycles, LC, which do not have any non-trivial spatial symmetry. Figure 28 shows the time evolution of the leading modal kinetic energies and $w(0.98,\ 0,\ -0.4\Gamma)$ for LC at $(\Gamma,\ Re)=(1.90,\ 275)$. Unlike the pulse wave states, LC does not exhibit slow–fast dynamics. The period in w is $2T_E$, twice the period in the modal energies. This suggests that like PWo, LC has a space–time symmetry. Figure 29 shows snap-shots of w–w_0 isosurfaces and of w contours at $z=0$, and together with the associated online movie 7, these allows us to determine the space–time symmetry of LC. Just like with PWo, applying $\mathcal{H}_\gamma$, for any γ, followed by the rotation $\mathcal{R}_{\phi-2\gamma}$ for a specific ϕ, to LC at any time t_0 results in LC at t_0+T_E. To better illustrate this space–time symmetry and to provide a way to determine ϕ for a given γ, we defined a symmetry measure

$$S=\|\mathcal{R}_{\phi-2\gamma}\mathcal{H}_\gamma\boldsymbol{u}-\mathcal{T}_{T_E}\boldsymbol{u}\|_2. \tag{3.1}$$

https://doi.org/10.1017/jfm.2017.103 Published online by Cambridge University Press

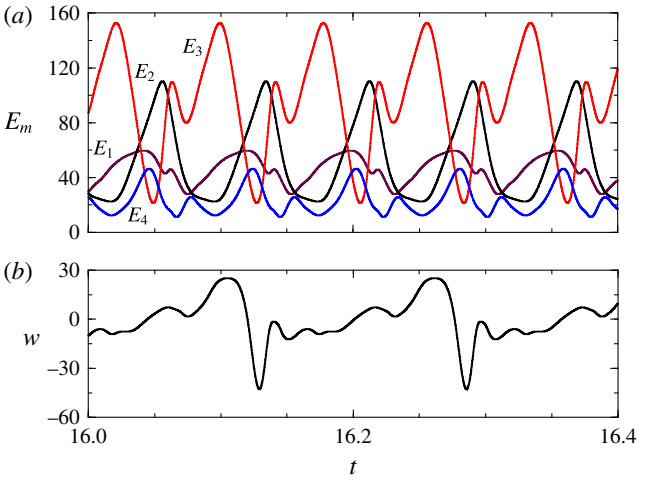


FIGURE 28. (Colour online) Time series of (*a*) modal kinetic energies E_1, E_2, E_3 and E_4 and (*b*) $w(0.98, 0, -0.4\Gamma)$ for LC at $(\Gamma, Re) = (1.9, 275)$.

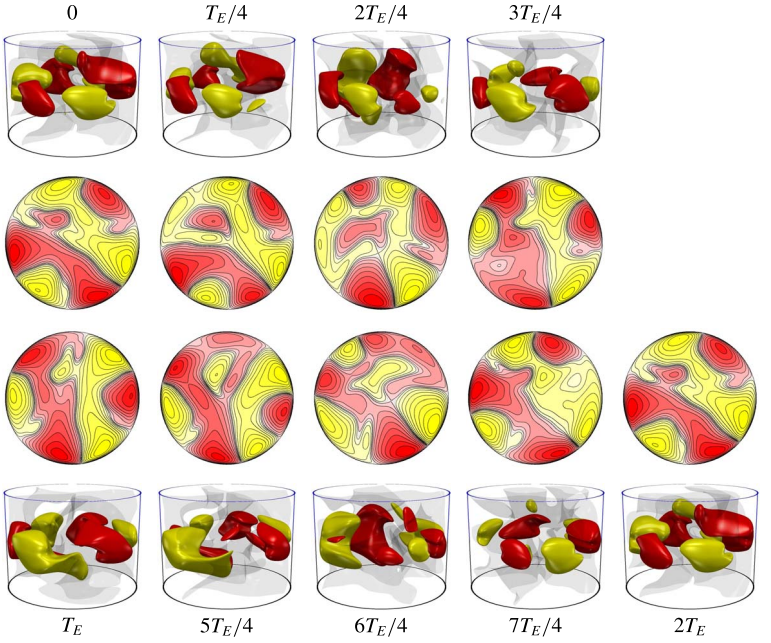


FIGURE 29. (Colour online) Snapshots of w–w_0 isosurfaces and w contours at $z = 0$ over $2T_E$ relative to an arbitrary reference time for LC at $(\Gamma, Re) = (1.90, 275)$. See the online movie 7 for an animation of isosurfaces of w–w_0.

Without loss of generality, figure 30 shows the symmetry measure S, calculated for a PWo state and a LC state when $\mathcal{H}_0$ is applied and considering $\phi \in [0, 2\pi]$. The symmetry measure is zero only for a specific $\phi = \phi_0$ (for PWo, $S = 0$ also for $\phi = \phi_0 \pm \pi$ because PWo is $\mathcal{R}_\pi$ symmetric). For any other γ, $S = 0$ at $\phi = \phi_0 - 2\gamma$. Apart from not having slow–fast behaviour, the other main difference between LC and PWo is that

https://doi.org/10.1017/jfm.2017.103 Published online by Cambridge University Press

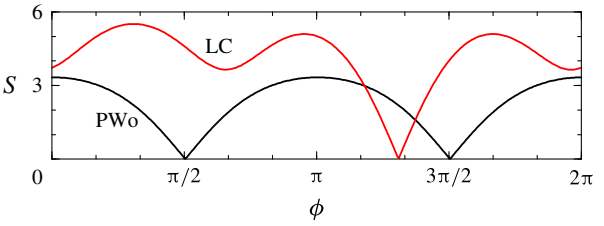


FIGURE 30. (Colour online) Variation of the symmetry measure S, using $\mathcal{H}_0$, with the rotation angle ϕ for PWo at $(\Gamma, Re) = (1.50, 210)$ and LC at $(\Gamma, Re) = (1.90, 275)$.

while both have comparable levels of E_2, for LC the level of E_3 is significantly larger than any other E_m most of the time, and this leads to LC not having any non-trivial spatial symmetry.

In summary, LC has invariances $\mathcal{T}_{2T_E}\boldsymbol{u} = \boldsymbol{u}$ and $\mathcal{T}_{T_E}\boldsymbol{u} = \mathcal{R}_{\phi-2\gamma}\mathcal{H}_\gamma\boldsymbol{u}$ for γ arbitrary and a given ϕ.

4. Discussion and conclusions

The dynamics of the flow in the split counter-rotating cylinder is dominated by the $O(2)$ symmetry of the system. The $O(2)$ symmetric basic state consists of two counter-rotating bodies of fluid, each completely contained within their respective half-cylinders, separated by a plane at the cylinder mid-height to which the vortex lines are tangential. The vortex lines being tangential to the mid-plane results in an azimuthal shear layer that also has a radial jet profile due to the vortex line bending. This basic state configuration becomes unstable with increasing counter rotation (quantified non-dimensionally by Re); the critical Re is smaller for larger cylinder aspect ratios Γ. The primary instabilities are circle-pitchfork bifurcations, spawning group orbits of steady states Sm with azimuthal wavenumbers m. The value of m depends on Γ, and for the range considered ($\Gamma \in [0.5, 2.0]$), m ranges from 6 to 2. There are a number of codim-2 points where two curves of circle-pitchfork bifurcations cross in (Γ, Re) parameter space, one curve corresponding to azimuthal wavenumber m and the other to $m + 1$. We have studied in detail the dynamics in the neighbourhood of the 2 : 3 codim-2 point, and the resulting mode interactions are well described by the associated normal form.

Further away in parameter space from the primary circle-pitchfork bifurcations, we have found a number of other bifurcations and states. Some of these states are unstable due to broken symmetries, and by computing in the appropriate symmetric subspaces we have been able to study their dynamics. We have found rotating waves and direction reversing waves that result from either steady or Hopf bifurcations breaking the involution $\mathcal{H}$ symmetry of the Sm from which they bifurcate. These time-periodic states are typical of $O(2)$ symmetric systems. However, over much of the parameter space studied, these are not the predominant unsteady states found. Instead, we find that a variety of pulse wave states dominate the unsteady flow regimes. These are primarily characterized by slow–fast dynamics, with the slow phase corresponding to a particular orientation of a steady non-axisymmetric state, typically S2, and the fast phase corresponds to a rapid shift to a different orientation in the S2 group. Some pulse waves (PWs and PWo) reside in the symmetric subspace with only even Fourier azimuthal modes, while others (PWa) do not. We have also found other limit cycle solutions. All of these can be viewed as different choreographies as the vortex

https://doi.org/10.1017/jfm.2017.103 Published online by Cambridge University Press

lines from one half of the cylinder try to penetrate into the other half, and the two sets of counter-rotating vortex lines negotiate their respective penetrations via flow configurations with different spatio-temporal symmetries.

All of the dynamics we have described is inherently related to how the $O(2)$ symmetry of the system is broken as Re and Γ are varied. The $O(2)$ symmetry owes its presence to the exact counter rotation of the two halves of the cylinder. Any slight difference in the rotation rates or the cylinder not being exactly split in half would result in the system only having $SO(2)$ symmetry. This then raises the question of how robust is the dynamics reported to slight imperfections. In the related von Kármán swirling flow, Nore *et al.* (2005) showed experimentally that much of the $O(2)$-related dynamics persists in the face of experimental imperfections and noise. The details of the basic state and its bifurcations for the von Kármán swirling flow differ from those of the split-cylinder flow, primarily due to the viscous drag from the stationary sidewall leading to very different vortex line distributions in the basic state and consequently undergoing different bifurcations. Yet, there are many similarities between the two flows and this is due to both systems being $O(2)$ symmetric. In both cases the basic state first loses stability via circle-pitchfork bifurcations to three-dimensional steady states Sm, but the azimuthal wavenumber m in the two cases differs. In both cases there are mode interactions where two circle-pitchfork bifurcations occur simultaneously, and these codim-2 points organize the dynamics over a sizable region of parameter space, displaying various rotating and pulse waves. Given the experimentally observed robustness of the $O(2)$ dynamics in the von Kármán swirling flow, it would be of interest to determine the effects of imperfections on the split-cylinder flow. In particular, the pulse waves can be viewed as a dynamic where the flow is a structure pinned to one particular orientation undergoing a very slow change until it de-pins and then quickly pins to another orientation. We found that the pulse waves PWa cease to exist via a SNIC bifurcation, whereby the structure remains pinned in a particular orientation indefinitely. Pinning and depinning of rotating waves in $SO(2)$ differentially rotating systems have also been reported and the role of imperfect symmetry has been investigated (Abshagen *et al.* 2008; Lopez & Marques 2009; Pacheco, Lopez & Marques 2011; Marques *et al.* 2013). These studies showed that SNIC bifurcations are predominant in the associated dynamics, but the details become extremely complicated. An investigation of imperfect $O(2)$ symmetry in the split-cylinder flow would be an interesting future exercise.

Acknowledgement

This work was supported by the US National Science Foundation grant CBET-1336410.

Supplementary movies

Supplementary movies are available at https://doi.org/10.1017/jfm.2017.103.

REFERENCES

ABSHAGEN, J., HEISE, M., HOFFMANN, CH. & PFISTER, G. 2008 Direction reversal of a rotating wave in Taylor–Couette flow. *J. Fluid Mech.* **607**, 199–208.

ARMBRUSTER, D., GUCKENHEIMER, J. & HOLMES, P. 1988 Heteroclinic cycles and modulated travelling waves in systems with $O(2)$ symmetry. *Physica* D **29**, 257–282.

https://doi.org/10.1017/jfm.2017.103 Published online by Cambridge University Press

BATCHELOR, G. K. 1951 Note on a class of solutions of the Navier–Stokes equations representing steady rotationally-symmetric flow. *Q. J. Mech. Appl. Maths* **4**, 29–41.

BLACKBURN, H. M. & LOPEZ, J. M. 2000 Symmetry breaking of the flow in a cylinder driven by a rotating end wall. *Phys. Fluids* **12**, 2698–2701.

BLACKBURN, H. M. & LOPEZ, J. M. 2002 Modulated rotating waves in an enclosed swirling flow. *J. Fluid Mech.* **465**, 33–58.

BOURGOIN, M., MARIÉ, L., PÉTRÉLIS, F., GASQUET, C., GUIGON, A., LUCIANI, J.-B., MOULIN, M., NAMER, F., BURGUETE, J., CHIFFAUDEL, A. *et al.* 2002 Magnetohydrodynamics measurements in the von Kármán sodium experiment. *Phys. Fluids* **14**, 3046–3058.

COULLET, P. & IOOSS, G. 1990 Instabilities of one-dimensional cellular patterns. *Phys. Rev. Lett.* **64**, 866–869.

CRAWFORD, J. D & KNOBLOCH, E. 1991 Symmetry and symmetry-breaking bifurcations in fluid dynamics. *Annu. Rev. Fluid Mech.* **23**, 341–387.

CRESPO DEL ARCO, E., SÁNCHEZ-ÁLVAREZ, J. J., SERRE, E., DE LA TORRE, A. & BURGUETE, J. 2009 Numerical and experimental study of the time-dependent states and the slow dynamics in a von Kármán swirling flow. *Geophys. Astrophys. Fluid Dyn.* **103**, 163–177.

DANGELMAYR, G. 1986 Steady-state mode interactions in the presence of $O(2)$-symmetry. *Dyn. Stab. Syst.* **1**, 159–185.

FAUVE, S., DOUADY, S. & THUAL, O. 1991 Drift instabilities of cellular patterns. *J. Phys. II* **1**, 311–322.

GAUTHIER, G., GONDRET, P., MOISY, F. & RABAUD, M. 2002 Instabilities in the flow between co- and counter-rotating disks. *J. Fluid Mech.* **473**, 1–21.

GIESECKE, A., STEFANI, F. & BURGUETE, J. 2012 Impact of time-dependent nonaxisymmetric velocity perturbations on dynamo action of von Kármán-like flows. *Phys. Rev.* E **86**, 066303.

GUTIERREZ-CASTILLO, P. & LOPEZ, J. M. 2015 Instabilities of the sidewall boundary layer in a rapidly rotating split cylinder. *Eur. J. Mech. (*B*/Fluids)* **52**, 76–84.

HIGUERA, M., RIECKE, H. & SILBER, M. 2004 Near-resonant steady mode interaction: periodic, quasi-periodic, and localized patterns. *SIAM J. Appl. Dyn. Syst.* **3**, 463–502.

JONES, C. A. & PROCTOR, M. R. E. 1987 Strong spatial resonance and travelling waves in Bénard convection. *Phys. Rev.* A **121**, 224–228.

KNESS, M., TUCKERMAN, L. S. & BARKLEY, D. 1992 Symmetry-breaking bifurcations in one-dimensional excitable media. *Phys. Rev.* A **46**, 5054–5062.

KNOBLOCH, E. 1996 Symmetry and instability in rotating hydrodynamic and magnetohydrodynamic flows. *Phys. Fluids* **8**, 1446–1454.

KRUPA, M. 1990 Bifurcations of relative equilibria. *SIAM J. Math. Anal.* **21**, 1453–1486.

LANDSBERG, A. S. & KNOBLOCH, E. 1991 Direction-reversing traveling waves. *Phys. Rev.* A **159**, 17–20.

LAUNDER, B., PONCET, S. & SERRE, E. 2010 Laminar, transitional, and turbulent flows in rotor-stator cavities. *Annu. Rev. Fluid Mech.* **42**, 229–248.

LOPEZ, J. M. 1998 Characteristics of endwall and sidewall boundary layers in a rotating cylinder with a differentially rotating endwall. *J. Fluid Mech.* **359**, 49–79.

LOPEZ, J. M. 2006 Rotating and modulated rotating waves in transitions of an enclosed swirling flow. *J. Fluid Mech.* **553**, 323–346.

LOPEZ, J. M. & GUTIERREZ-CASTILLO, P. 2016 Three-dimensional instabilities and inertial waves in a rapidly rotating split-cylinder flow. *J. Fluid Mech.* **800**, 666–687.

LOPEZ, J. M., HART, J., MARQUES, F., KITTELMAN, S. & SHEN, J. 2002 Instability and mode interactions in a differentailly-driven rotating cylinder. *J. Fluid Mech.* **462**, 383–409.

LOPEZ, J. M. & MARQUES, F. 2004 Mode competition between rotating waves in a swirling flow with reflection symmetry. *J. Fluid Mech.* **507**, 265–288.

LOPEZ, J. M. & MARQUES, F. 2009 Centrifugal effects in rotating convection: nonlinear dynamics. *J. Fluid Mech.* **628**, 269–297.

MARQUES, F., GELFGAT, A. YU. & LOPEZ, J. M. 2003 A tangent double Hopf bifurcation in a differentially rotating cylinder flow. *Phys. Rev.* E **68**, 016310.

https://doi.org/10.1017/jfm.2017.103 Published online by Cambridge University Press

MARQUES, F., MESEGUER, A., LOPEZ, J. M., PACHECO, J. R. & LOPEZ, J. M. 2013 Bifurcations with imperfect $SO(2)$ symmetry and pinning of rotating waves. *Proc. R. Soc. Lond.* A **469**, 20120348.

MERCADER, I., BATISTE, O. & ALONSO, A. 2010 An efficient spectral code for incompressible flows in cylindrical geometries. *Comput. Fluids* **39**, 215–224.

MOISY, F., DOARÉ, O., PASUTTO, T., DAUBE, O. & RABAUD, M. 2004 Experimental and numerical study of the shear layer instability between two counter-rotating disks. *J. Fluid Mech.* **507**, 175–202.

MONCHAUX, R., BERHANU, M., BOURGOIN, M., MOULIN, M., ODIER, PH., PINTON, J.-F., VOLK, R., FAUVE, S., MORDANT, N., PÉTRÉLIS, F. *et al.* 2007 Generation of a magnetic field by dynamo action in a turbulent flow of liquid sodium. *Phys. Rev. Lett.* **98**, 044502.

NORE, C., MOISY, F. & QUARTIER, L. 2005 Experimental observation of near-heteroclinic cycles in the von Kármán swirling flow. *Phys. Fluids* **17**, 064103.

NORE, C., TARTAR, M., DAUBE, O. & TUCKERMAN, L. S. 2004 Survey of instability thresholds of flow between exactly counter-rotating disks. *J. Fluid Mech.* **511**, 45–65.

NORE, C., TUCKERMAN, L. S., DAUBE, O. & XIN, S. 2003 The $1:2$ mode interaction in exactly counter-rotating von Kármán swirling flow. *J. Fluid Mech.* **477**, 51–88.

NORE, C., WITKOWSKI, L. M., FOUCAULT, E., PÉCHEUX, J., DAUBE, O. & LE QUÉRÉ, P. 2006 Competition between axisymmetric and three-dimensional patterns between exactly counter-rotating disks. *Phys. Fluids* **18**, 054102.

PACHECO, J. R., LOPEZ, J. M. & MARQUES, F. 2011 Pinning of rotating waves to defects in finite Taylor–Couette flow. *J. Fluid Mech.* **666**, 254–272.

PORTER, J. & KNOBLOCH, E. 2001 New type of complex dynamics in the $1:2$ spatial resonance. *Physica* D **159**, 125–154.

RAVELET, F., MARIE, L., CHIFFAUDEL, A. & DAVIAUD, F. 2004 Multistability and memory effect in a highly turbulent flow: experimental evidence for a global bifurcation. *Phys. Rev. Lett.* **93**, 164501.

RAVELET, F., MONCHAUX, R., AUMAÎTRE, S., CHIFFAUDEL, A., DAVIAUD, F., DUBRULLE, B., BOURGOIN, M., ODIER, PH., PLIHON, N., PINTON, J.-P. *et al.* 2008 Chaotic dynamos generated by a turbulent flow of liquid sodium. *Phys. Rev. Lett.* **101**, 074502.

ROTT, N. & LEWELLEN, W. S. 1966 Boundary layers and their interactions in rotating flows. *Prog. Aerosp. Sci.* **7**, 111–144.

STEWARTSON, K. 1953 On the flow between two rotating coaxial disks. *Proc. Camb. Phil. Soc.* **49**, 333–341.

STROGRATZ, S. H. 1994 *Nonlinear Dynamics and Chaos*. Addison-Wesley.

DE LA TORRE, A. & BURGUETE, J. 2007 Slow dynamics in a turbulent von Kármán swirling flow. *Phys. Rev. Lett.* **99**, 054101.

ZANDBERGEN, P. J. & DIJKSTRA, D. 1987 Von Kármán swirling flows. *Annu. Rev. Fluid Mech.* **19**, 465–491.

https://doi.org/10.1017/jfm.2017.103 Published online by Cambridge University Press